Available online at www.sciencedirect.com

SciVerse ScienceDirect

Acta Materialia 61 (2013) 6132–6152

Acta MATERIALIA

www.elsevier.com/locate/actamat

Segregation engineering enables nanoscale martensite to austenite phase transformation at grain boundaries: A pathway to ductile martensite

D. Raabe *, S. Sandlöbes, J. Millán, D. Ponge, H. Assadi, M. Herbig, P.-P. Choi

Department for Microstructure Physics and Alloy Design, Max-Planck-Institut für Eisenforschung, Max-Planck-Strasse 1, 40237 Düsseldorf, Germany

Received 14 May 2013; received in revised form 22 June 2013; accepted 30 June 2013
Available online 6 August 2013

Abstract

In an Fe–9 at.% Mn maraging alloy annealed at 450 °C reversed allotriomorphic austenite nanolayers appear on former Mn decorated lath martensite boundaries. The austenite films are 5–15 nm thick and form soft layers among the hard martensite crystals. We document the nanoscale segregation and associated martensite to austenite transformation mechanism using transmission electron microscopy and atom probe tomography. The phenomena are discussed in terms of the adsorption isotherm (interface segregation) in conjunction with classical heterogeneous nucleation theory (phase transformation) and a phase field model that predicts the kinetics of phase transformation at segregation decorated grain boundaries. The analysis shows that strong interface segregation of austenite stabilizing elements (here Mn) and the release of elastic stresses from the host martensite can generally promote phase transformation at martensite grain boundaries. The phenomenon enables the design of ductile and tough martensite.
© 2013 Acta Materialia Inc. Published by Elsevier Ltd. All rights reserved.

Keywords: Phase transformation; Austenite; Atom probe tomography; Grain boundary segregation; Austenite reversion

1. Introduction

Strong, damage-tolerant, and functional steels are the backbone for innovation in the fields of manufacturing, energy, transportation, and safety. Examples are Fe–Cr steels for reduced emission turbines, reduced weight and high strength Fe–Mn steels for light weight and safe mobility applications, magnetic Fe–Si steels for low loss electrical motors and generators, and stainless steels for fission, fusion, and direct solar thermal power plants. These examples indicate the necessity of developing improved high strength and yet ductile steels. Most hardening mechanisms, however, such as those enabled by solutes, dislocations, and precipitates, albeit leading to high strength, often reduce ductility, rendering the material brittle and susceptible to failure. This phenomenon is known as the inverse strength–ductility problem [1–3].

In this context a reduction in the average grain size offers a pathway to increase both the strength and toughness of steels [4–8]. In this work we develop this concept further in that we combine this strategy with manipulation of the individual interfaces by grain boundary segregation and local phase transformation. More specifically, we enable grain boundaries in high strength steels not only as barriers against dislocation motion but also as regions where segregation and nanoscale phase transformation can take place. Such locally transformed regions (here martensite to austenite reversion at martensite grain boundaries) can act as compliance layers or mechanical buffer zones impeding, for instance, crack penetration among lath martensite lamellae.

It should be mentioned that for this concept to work the exact nature of the decorated and subsequently transformed martensite grain boundaries is not decisive.

* Corresponding author.
E-mail address: d.raabe@mpie.de (D. Raabe).

1359-6454/$36.00 © 2013 Acta Materialia Inc. Published by Elsevier Ltd. All rights reserved.
http://dx.doi.org/10.1016/j.actamat.2013.06.055

Martensite can reveal different types of interfaces which could in principle all be manipulated in the way described, namely prior austenite, packet, block, or lath boundaries, which all have different energies, structures, misorientations, mechanics, and segregation properties [9–13]. In the current alloy lath martensite boundaries are the most relevant and frequent type of interfaces [2]. They are preferably susceptible to crack penetration owing to their low mutual misorientation, hence reversing them to an austenite buffer layer might be of specific benefit in the current alloy design strategy.

To utilize this concept we first have to better understand the susceptibility of grain boundaries to solute decoration and the resulting property changes [14–29]. This phenomenon, referred to as grain boundary segregation, is characterized by the redistribution of solutes from the grain interiors to the grain boundaries [14–19]. Solute concentrations on grain boundaries can exceed the solubility inside grains, sometimes by a factor of 2–3, and sometimes even by more than an order of magnitude [20,22,25]. A rough approximation of the segregation tendency of a solute is its inverse bulk solubility, namely the smaller the bulk solubility, the higher the enrichment factor at the interface [20,22,25].

When grain boundary segregation occurs, either via inherited solute decoration from preceding processing (i.e. decoration of former austenite grain boundaries) or upon modest tempering after quenching (i.e. decoration of ferrite or martensite grain boundaries), different scenarios are conceivable [20–37]. First, segregation might enhance coherence and preferential bonding at the interface (grain boundary strengthening). Second, the reverse might be true, namely a further loss of coherence and weaker or unfavourably directed bonding at the interface (grain boundary weakening). Third, segregation could lead to phase transformation of the grain boundary (grain boundary phase transformation). Fourth, segregation could promote formation of one or more second phases at the decorated interface (grain boundary precipitation, complexion, phase formation at grain boundaries). Fifth, discontinuous precipitation might be initiated.

Besides these possible direct structural changes in the intrinsic grain boundary properties due to segregation, their energy is also affected. The Gibbs adsorption isotherm, when applied to segregation at internal interfaces, quantifies the reduction in the total system free energy as a driving force for equilibrium segregation [15,19]. Since bulk grain depletion and the associated free energy change is negligible in this context, the main thermodynamic driving force for solute segregation to grain boundaries is a reduction in the interface free energy. This also affects the relationship between segregation and ductility, since a drop in the grain boundary energy reduces the driving force for grain growth [26–29]. Hence, materials with reduced grain boundary energy can, under the same thermomechanical treatment as used for materials without grain boundary segregation, have a smaller and at the same time rather stable grain size. This can improve both strength and toughness, provided the specific type of segregation does not lead to grain boundary embrittlement [30,31].

In the present study we address one specific phenomenon, namely the segregation of solute Mn to martensite grain boundaries [2]. This includes all possible kinds of martensite grain boundaries, i.e. prior austenite boundaries, block boundaries, packet boundaries and lath boundaries [9–13,32], of a quenched and tempered Fe–Mn alloy and the associated nanoscale phase transformation of the decorated grain boundary region from martensite to austenite. This martensite to austenite reversion occurs at a temperature far below the bulk retransformation temperature.

Such interactions among grain boundary structure, segregation, and confined phase transformation open opportunities for the nanoscale engineering of damage-tolerant high strength steels, since all these mechanisms can be realized through simple alloying and thermomechanical processing strategies [2].

The challenge here lies in documenting both segregation and nanoscale phase transformation at the same interface. This requires the combined use of characterization methods with near atomic scale chemical and structural resolution. Here we use atom probe tomography in conjunction with transmission electron microscopy (TEM) diffraction. We term this new approach of jointly manipulating the structure and composition of grain boundaries via segregation plus phase transformation "segregation engineering" (Fig. 1) [33–37].

2. Experimental procedure

2.1. Alloy synthesis

An Fe–9Mn–1.9Ni–0.6Mo–1.1Ti–0.33Al–0.1Si–0.05C (at.%) maraging steel was melted and cast as round billets of 1 kg weight in a vacuum induction furnace (the term "maraging" derives from martensite + aging). Since high Mn steels tend to show pronounced segregation and form heterogeneous microstructures after casting the material was homogenized by two processing cycles consisting of re-austenitization and hot deformation. After that cold rolling, recrystallization, and a final solution heat treatment were performed in an Ar atmosphere at 1050 °C for 30 min, followed by water quenching. Final ageing was conducted at 450 °C for 48 h. Details have been previously published [14,38]. Thermodynamic calculations were carried out using Thermo-Calc in conjunction with the TCFE6 database [38–40].

2.2. Transmission electron microscopy

Discs of 3 mm diameter and 1 mm thickness were cut by wire erosion. They were mechanically ground to a thickness of 70–90 μm and subsequently electropolished until perforation (Struers Tenupol-5). The electrolyte was a

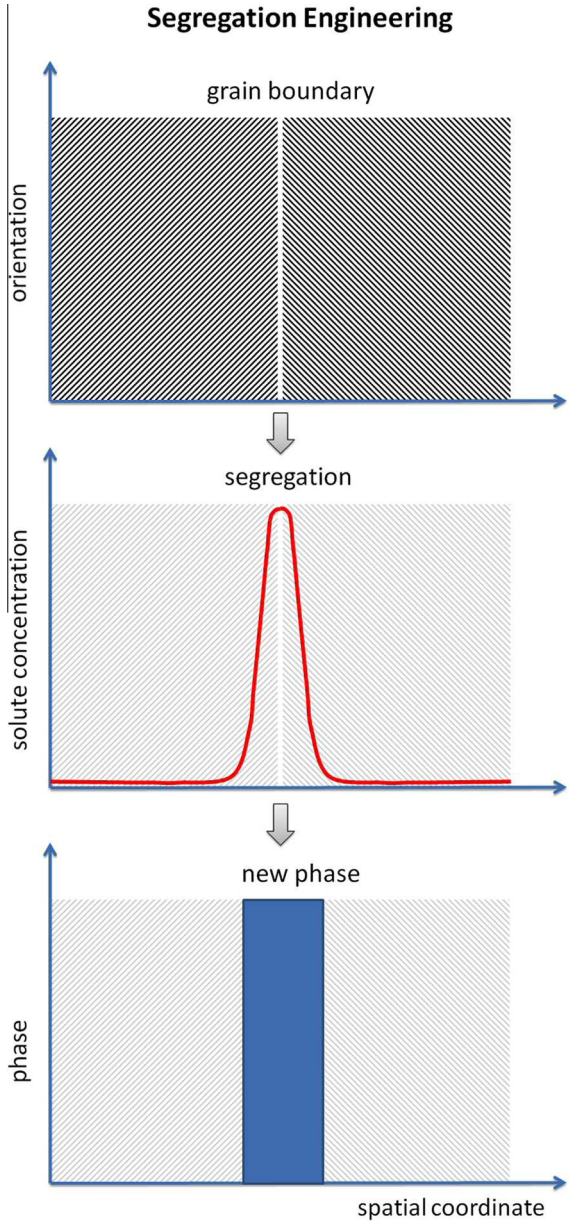

Fig. 1. Principle of "segregation engineering". The approach is based on grain boundary segregation followed by nanoscale phase transformation of the decorated grain boundary region. Here we use Mn segregation to martensite grain boundaries followed by segregation-assisted and distortion-assisted martensite to austenite reversion at these grain boundaries.

solution of 6% perchloric acid, 30% 1-butanol glycol ester and 64% methanol. TEM observations were performed in a Philips CM20 with LaB_6 filament operated at an acceleration voltage of 200 keV.

2.3. Atom probe tomography (APT)

Atomic scale composition analysis of the material after ageing was conducted using atom probe tomography (APT). Atom probe specimens were prepared by standard two step electrochemical polishing [41–50]. Square rods with a 0.3×0.3 mm cross-section and 20 mm long were cut from the aged sample. In the first electrochemical polishing step rods of square cross-section were roughly sharpened using a solution of 9 vol.% perchloric acid in glacial acetic acid. The second step was done using a solution of 2 vol.% perchloric acid in butoxyethanol. Final sharpening by focused ion beam (FIB) milling (using a FEI Helios Nanolab 600 dual beam FIB) was carried out in order to obtain an initial sample tip radius of <50 nm. Voltage-pulsed APT was performed using a local electrode atom probe (LEAP 3000X HR™, Imago Scientific Instruments) at a specimen temperature of about 90 K. The voltage pulse fraction was set at 0.2, with a pulse frequency of 200 kHz. The detection rate amounted to 5 atoms per 1000 pulses. Data analysis was performed using the IVAS® software of Imago Scientific Instruments. The reconstruction of three-dimensional (3-D) atom maps was carried out using an evaporation field constant of 33 V nm^{-1}, which corresponds to that of pure Fe at 77 K [41].

3. Experimental results

3.1. EBSD and TEM analysis of the quenched and aged state

Fig. 2 shows electron backscatter diffraction (EBSD) and transmission electron microscopy (TEM) micrographs of the microstructure of a quenched plus aged specimen (48 h at 450 °C). The phase distribution map (left hand image) reveals that fast quenching to room temperature subsequent to austenitization leads to a martensite microstructure. The inverse pole figure map and the TEM micrograph show lath martensite [9–13,32]. A martensitic microstructure of this material and a high frequency of lath boundaries after quenching without ageing were shown in Raabe et al. [2]. Most of the interfaces analysed below by APT were prepared by site-specific FIB from small angle (lath) interfaces.

3.2. TEM analysis

In tempered specimens (450 °C, 48 h) we observe layers with a thickness of 10–15 nm at the martensite block boundaries and at the martensite lath boundaries. These zones are mostly devoid of precipitates, which as a rule only form inside martensite grains (see Fig. 3a). Exceptions can apply in cases where the particle first formed inside the martensite before the zone surrounding it became transformed to austenite. The inset in Fig. 3a shows an enlarged image of such a region. The micrograph reveals that this interface zone is characterized by a nanoscaled double layer, where the two individual films are separated from each other by an internal interface. This interface is not visible over the entire length of the double layer in one single micrograph. It appears at different positions along the grain boundary when tilting the sample. This effect is due to a slight bending of the TEM foil, which causes minor orientation differences along the longitudinal axis of the

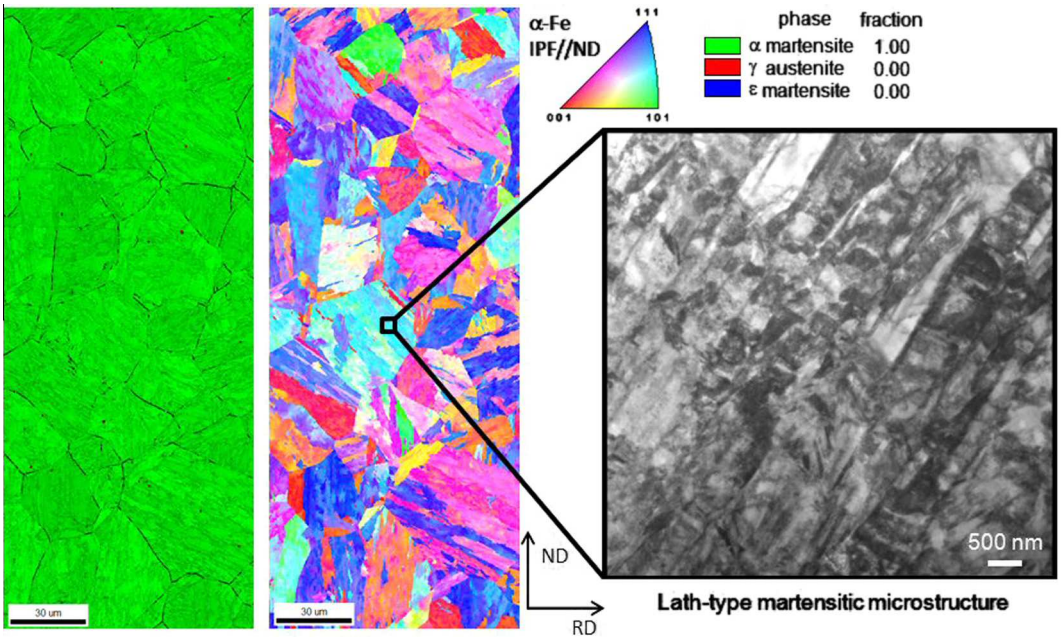

Fig. 2. Microstructure of a precipitation hardened Fe–9 at.% Mn maraging steel in the aged condition (450 °C, 48 h). (Left) EBSD phase map showing a fully martensitic structure. The prior austenite grain boundaries are marked by black lines using the software OIM. (Centre) Inverse pole figure texture map displaying crystal orientations in terms of the {*hkl*} Miller indices parallel to the normal direction (ND). (Right) Bright field TEM image of the underlying nanostructure of the material revealing lath-type martensite.

interface with respect to the incident electron beam. Fig. 3b shows a schematic image of the region.

After tilting the sample in such a way that both martensite grains are close to a major pole orientation selected area diffraction (SAD) patterns were taken from both the martensite grains and the double layer between them. The position of the SAD aperture and the corresponding SAD pattern are shown in Fig. 4. For better clarity, the SAD patterns are numbered: SADP 1, referring to the grain on the left-hand side; SADP 2–5, taken from both martensitic grains and the interfacial layers between them; SADP 6, showing the pattern of the martensite grain on the right-hand side. With a thickness of 30–50 nm in the inspection zone the TEM specimen is thin enough to obtain a clear pattern from the interfacial double layer and, thus, enable indexing of the diffraction patterns of the double layer. Super-structure reflections from the nanoprecipitates formed in the martensite are also visible (marked in Fig. 5). The nanoprecipitates have B2 structure, however, their detailed characterization is not discussed here.

Fig. 5 shows enlarged images of SADP 1, 3, and 6, respectively. The grain on the left-hand side of Figs. 3 and 4 is oriented near to the $[1\,1\,1]_{bcc}$ pole (Fig. 5a), while the orientation of the grain on the right-hand side is inclined towards the $[0\,0\,1]_{bcc}$ pole (Fig. 5b). In the latter images (Fig. 5b) the super-structure diffraction spots from the B2 ordered precipitates are also visible. The alloy has a very low carbon content, i.e. the martensite assumes a nearly body-centred cubic (bcc) structure. Hence, the SAD patterns show only small tetragonal distortion of the bcc lattice. SADP 2 (Fig. 5c) and 3 (Fig. 5d) were taken from a region containing both grains plus the interfacial double layer. The reflections of both martensite grains and of the intergranular double layer are visible. As marked in SADP 2 and 3 in Fig. 5, the intergranular double layer has face-centred cubic (fcc) structure (both thin layers) but the two abutting films have distinctly different crystallographic orientations.

In Fig. 5c (SADP 2) one of these orientations is highlighted. These fcc reflections exhibit a Kurdjumow–Sachs (K-S) orientation relationship of the corresponding austenite film with the adjoining martensite grain on the left-hand side. As indicated by the SAD pattern circle in Fig. 4, both, the thin fcc structured layer and the abutting left-hand side martensite grain contribute diffraction spots to SADP 2. This overlap enables us to conclude that the fcc reflections originate from the left-hand side layer of the interfacial double layer. As sketched in Fig. 5d (dashed light blue lines), the reflections obtained from the other intergranular layer are indexed as $[0\,1\,2]_{fcc}$ (not a major pole orientation). Whether a special orientation relationship of this right-hand side austenite layer to the adjacent right-hand side martensite grain exists could not be determined from these data. A schematic image of the structure of the martensite–austenite–martensite boundary region is given in Fig. 6.

Similar interfacial layers were observed at other martensite lath boundaries, but could not be indexed in most cases as either the grains were not favourably oriented for the procedure described here to be applicable or the TEM specimen was too thick to retrieve clear SAD patterns.

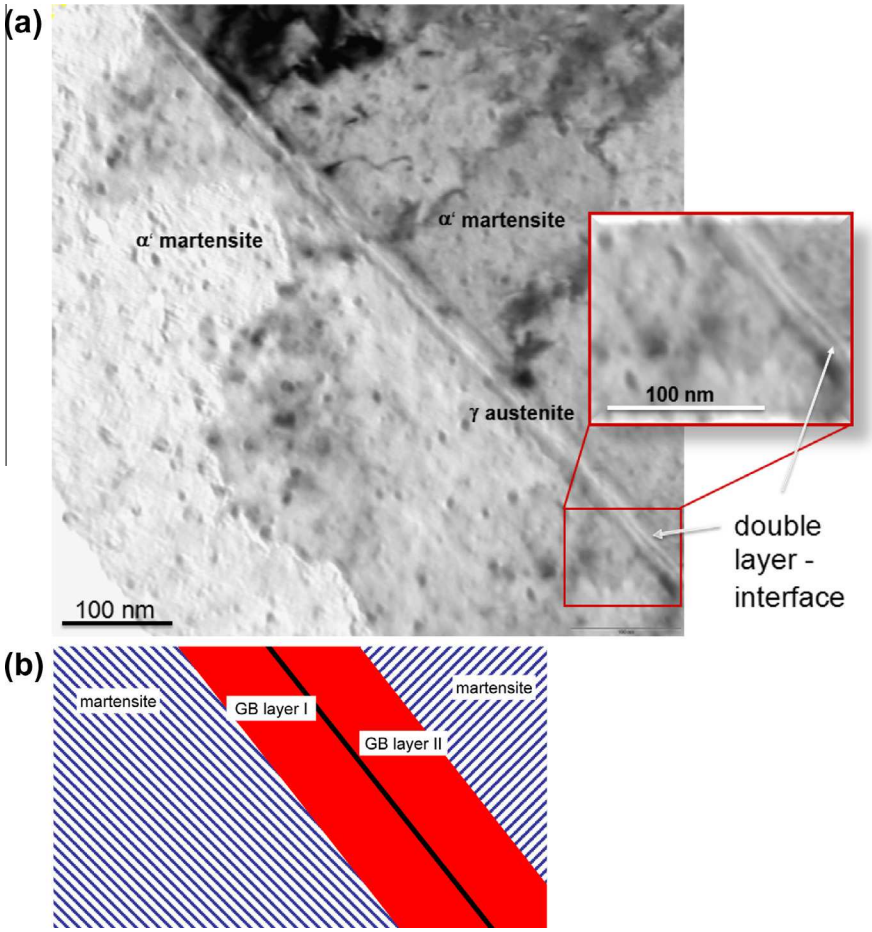

Fig. 3. (a) TEM bright field image of the interfacial double layer observed at a martensite–martensite grain boundary. (Inset) An enlarged image of the two nanolayers. (b) Schematic image of the observed grain boundary layers.

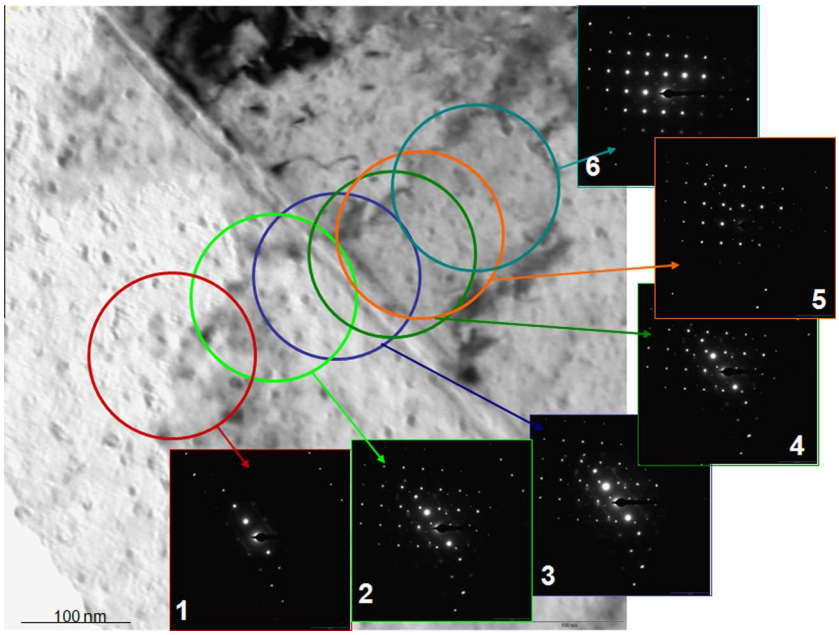

Fig. 4. TEM bright field image of the interfacial double layer and SAD patterns across the interface of the same microstructure shown in Fig. 3. The circles indicate the excitation zones which contribute to the SAD signals, i.e. the size of the circles correlate with the diameter of the SAD aperture.

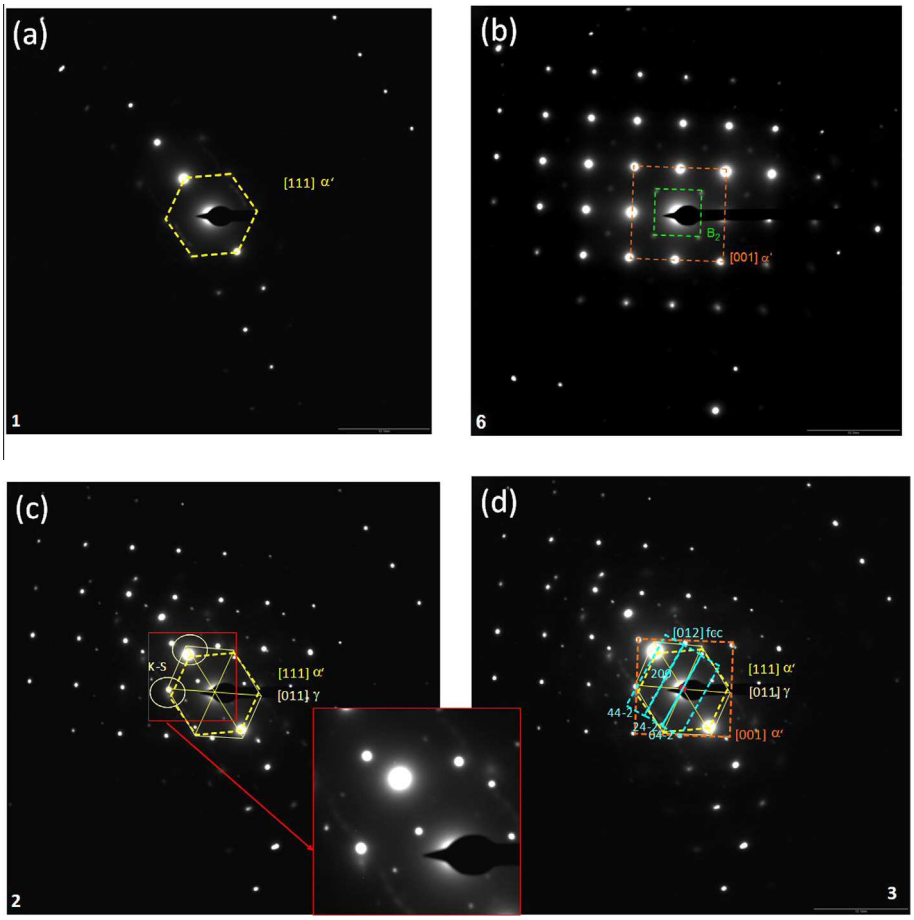

Fig. 5. SAD patterns of (a) the left hand grain (SADP 1), (b) the right hand grain (SADP 6) and (c and d) the two abutting interfacial layers (SADP 2). The left grain is near the $[1\,1\,1]_{bcc}$ orientation, the left grain near the $[0\,0\,1]_{bcc}$ orientation. The centre two interfacial layers are fcc.

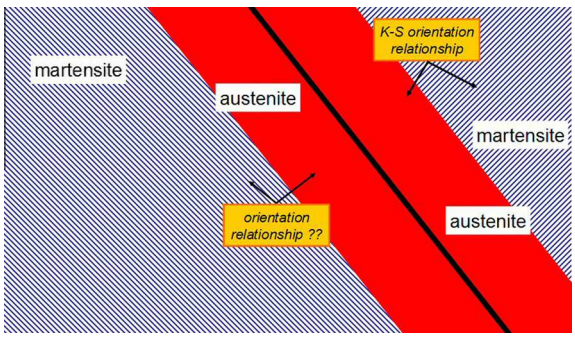

Fig. 6. Schematic view of the martensite–austenite–martensite boundary region.

3.3. Atom probe tomography analysis

Fig. 7 shows a 3-D atom probe tomography (APT) reconstruction of such a martensite–austenite–martensite grain boundary region. Following the TEM and SAD pattern structure analysis presented above we emphasize here that the region probed by APT includes the original martensite grains and the two associated thin austenite layers between them (Figs. 4 and 5). Mn atoms are displayed in yellow and Fe in blue. The chemical isoconcentration surfaces at 14 at.% Mn (threshold value to highlight Mn-enriched regions) are shown as yellow envelopes.

To quantify enrichment of the alloying elements in the martensite–austenite–martensite boundary region a selected area of the boundary region was analysed separately in more detail. A cylinder of 4 nm diameter was placed perpendicular to the interface plane (see Fig. 7a) and the one-dimensional concentration profile within this cylinder was integrated and is presented along the cylinder axis in the direction indicated by the black arrow. The individual element distribution maps of the alloying elements in the vicinity of the martensite–austenite–martensite boundary region are shown in Fig. 7b.

Fig. 8 shows the chemical gradients (in at.%) across the martensite–austenite–martensite grain boundary region that was analysed before by TEM (Figs. 4 and 5). The interface zone after tempering (450 °C, 48 h) is characterized by a complex chemical profile, more specifically by a large variation in the Mn content.

While the nominal bulk composition of the maraging steel was Fe–9Mn–1.9Ni–0.6Mo–1.1Ti–0.33Al–0.1Si–0.05C (at.%), the interface region revealed an enriched layer with a very high Mn concentration of ~22–23.5 at.%. Interestingly, in the centre zone of the interface

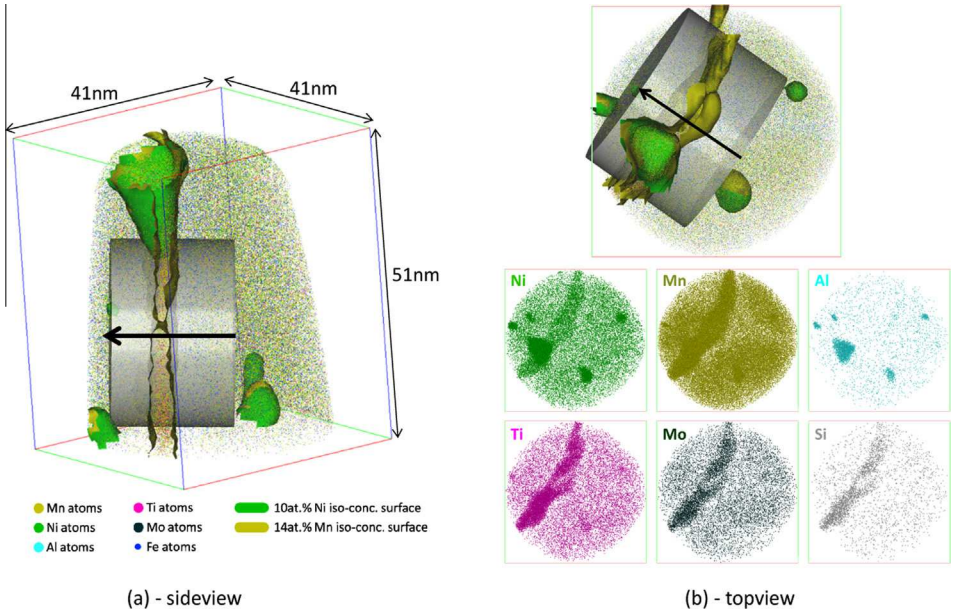

Fig. 7. APT results of the aged 9% Mn alloy (450 °C, 48 h). (a) 3-D side view of the dataset. Mn (yellow) and Ni (green) isoconcentration surfaces are marked to visualize the positions of the martensite–austenite–martensite interface region and the nanosize B2 precipitates (the latter being visible particularly due to Al accumulation in (b)). (b) Top view of the same martensite–austenite interface region with the corresponding element distribution maps revealing the accumulation of Ni, Mn, Ti, Mo and Si in the two phase region (bcc martensite, reversed fcc austenite). The nominal bulk composition of the maraging alloy is Fe–9Mn–1.9Ni–0.6Mo–1.1Ti–0.33Al–0.1Si–0.05C (at.%). (For interpretation of the references to colour in this figure legend, the reader is referred to the web version of this article.)

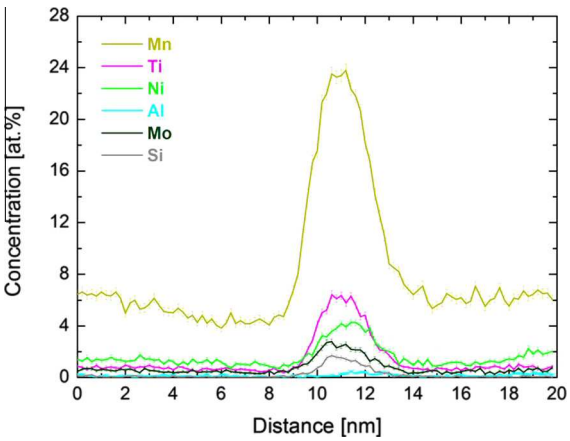

Fig. 8. Chemical gradients across the martensite–austenite–martensite interface region after tempering (450 °C, 48 h). The nominal composition of the alloy is Fe–9Mn–1.9Ni–0.6Mo–1.1Ti–0.33Al–0.1Si–0.05C (at.%). The Mn enrichment extends about 7 nm in thickness, while the Ti, Ni, Mo and Si enrichments only extend about 4 nm. The data also reveal the segregation of ferrite stabilizing elements, namely Ti, Mo, and Si. This would not occur if the decorated region was retained austenite.

Ti, Ni, Mo, and Si were also enriched (Figs. 7 and 8). This observation indicates that the probed grain boundary region did not contain retained austenite, since this would contradict the segregation of ferrite stabilizing elements such as Ti, Mo, and Si to this region during ageing (Table 1).

It should be considered that local magnification as well as interface inclination effects may lead to a slightly reduced sharpness of the concentration profiles, hence the exact lateral expansion of the enriched zone should be discussed with care. Calibration of the true expansion of the element-enriched zone can be achieved using the TEM analysis discussed above. It is important to note that the Mn content inside the martensite grains next to the Mn-enriched centre region (i.e. to the former martensite grain boundary) is lower by ~4–5 at.% compared with the average bulk martensite Mn concentration (9 at.%).

In order to demonstrate that the observed segregation and associated martensite to austenite transformation phenomena shown in Figs. 3–8 are not singular events

Table 1
Analysis of the grain boundary segregation data obtained by APT as shown in Figs. 7 and 8 in comparison with Thermo-Calc equilibrium calculations at the same reversion temperature (450 °C).

Element	Bulk composition (at.%)	Ferrite equilibrium composition[a] (at.%)	Austenite equilibrium composition[a] (at.%)	APT result at the interface (at.%)
Mn	9	2.78	28.40	20.7
Ni	1.9	0.15	7.36	3.2
Mo	0.6	0.63	0.49	2.2
Ti	1.1	1.27	0.58	5.2
Al	0.33	0.42	0.04	0.07
Si	0.1	0.11	0.08	1.4
C	0.05	0.00	0.21	0.0

The fact that not only Mn and Ni but also Mo, Ti, and Si are strongly segregated to the interface suggests that the region is not retained austenite but a martensite grain boundary.

[a] Thermo-Calc TCFE7, allowing only bcc and fcc phases, equilibrium calculation for 450 °C.

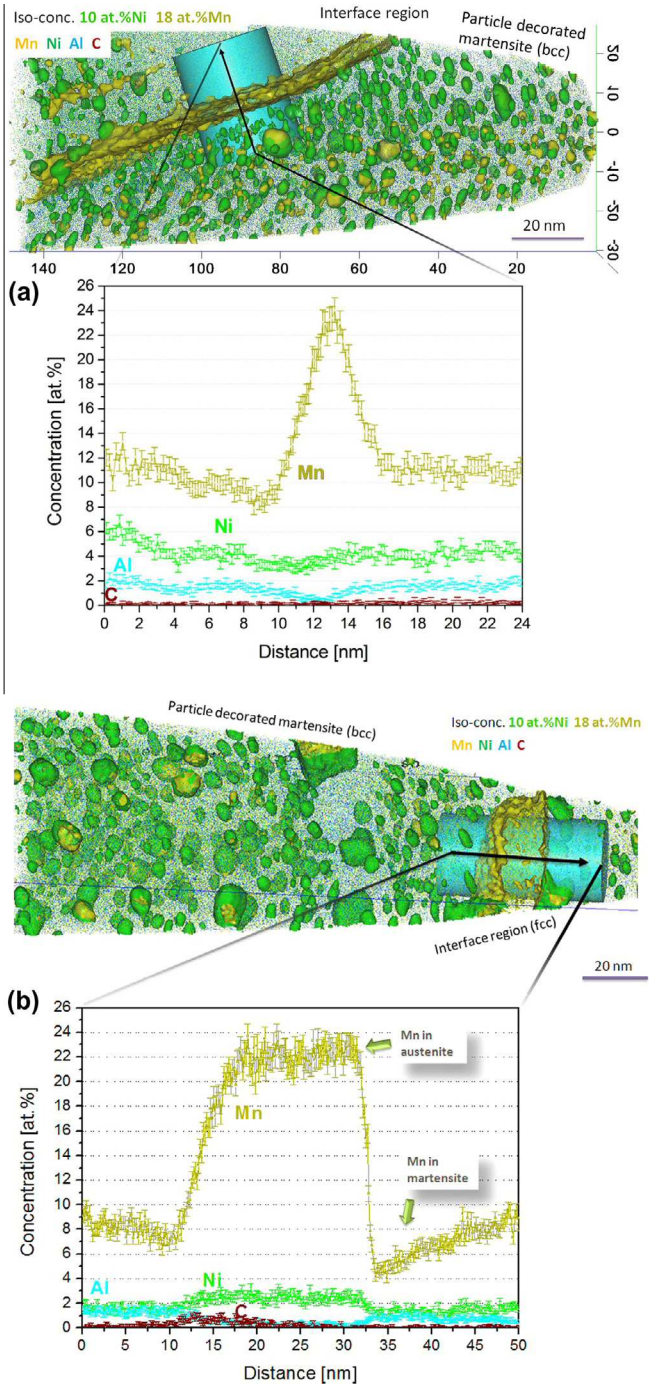

Fig. 9. (a) Mn decoration of a martensite–martensite grain boundary after tempering (450 °C, 48 h) of the alloy Fe–9Mn–1.9Ni–0.6Mo–1.1Ti–0.33Al–0.1Si–0.05C (at.%). The Mn enrichment is due to equilibrium segregation. The precipitates identify the martensitic phase (austenite does not form B2 type precipitates). (b) The same material in a more progressed state. The data show, similarly to Figs. 5–8, the onset of austenite formation and growth on a former martensite grain boundary in terms of a Mn gradient across the martensite–austenite–martensite region. The transformed volume is visible as a zone of constant Mn enrichment of about 22–23 at.%. Ni is also enriched, while Al is depleted, in this zone.

but were observed systematically in this material we display two more examples of the same phenomenon in Fig. 9. The first example (Fig. 9a) shows a situation where a lath boundary is decorated by equilibrium Mn segregation up to saturation level. The second example (Fig. 9b) shows, similarly to Figs. 5–8, the onset of austenite reversion plus growth on a former martensite grain boundary. The transformed region is visible in terms of a broadened zone of intense yet locally constant Mn enrichment of about 22–23 at.%. Ni is also enriched, while Al is depleted in the transformed region. The nanoparticles that formed during tempering of the quenched maraging steel are visible in both figures in terms of the Ni and Mn concentration envelopes and also the corresponding reflections in TEM, indicating mainly B2-type structures [38,56]. The precipitates, albeit not in focus here, are helpful, as they identify the martensitic regions. The results shown in Fig. 9b are particularly interesting, since they reveal not only austenite phase formation and growth at a former martensite interface but also near equilibrium partitioning of Mn (and the other elements) at the newly formed heterogeneous interface.

4. Discussion

4.1. Grain boundary segregation of Mn prior to local interface phase transformation

To describe the segregation of Mn to the martensite grain boundary we use the grain boundary segregation coefficient $\beta_{Mn} = X^{\varphi}_{Mn}/X^{B}_{Mn} = \beta_0 \exp(\Delta H^0_{Mn}/(RT))$, where X^{φ}_{Mn} is the Mn concentration in the grain boundary, X^{B}_{Mn} is the Mn concentration in the bulk martensite grain, β_0 is a temperature-independent pre-factor, and ΔH^0_{Mn} is the enthalpy of segregation [15,19]. The segregation coefficient is also often called the grain boundary enrichment factor.

Fig. 10 shows a compilation of some grain boundary segregation data for different binary systems from values published by Shea and Hondros [14–18], Lejček [20–22,25], and, regarding Mn in martensitic steel, from our own measurements conducted here and in previous works using APT [38,56] (arrow in Fig. 10). It includes the grain boundary enrichment factor relative to the bulk solubility of the same solute element for a number of steels. The diagram shows that the segregation of Mn in ferritic (martensitic) steel is similar to that of Ni. The segregation data obtained from our atom probe measurements show between 4 and 9 at.% Mn and between 20 and 24 at.% Mn enrichment inside the martensite grains and at the martensite grain boundaries, respectively.

Nikbakht et al. [57] worked on the grain boundary segregation of Mn with respect to the problem of isothermal embrittlement of Fe–8Mn alloys at 450 °C. They suggested that in their alloys brittle fracture was due to segregation of Mn to prior austenite grain boundaries. That work also suggested the possibility that Mn segregation to such specific prior austenite grain boundaries might support the initial formation of reverted austenite at such sites. This is clearly confirmed by our current results.

In another work Nasim et al. [58] showed by carefully conducted Auger spectroscopy that Mn segregated to the

grain boundaries in an Fe–8Mn alloy upon ageing at 450 °C. The Mn values that they observed were on average somewhat lower than the ones we observe here by APT: our current results reveal 20–24 at.% Mn enrichment at martensite grain boundaries, while their data showed values of about 18 at.% Mn (Fig. 11). The deviation is attributed to the different alloy composition and the different annealing times. Also, APT yields a higher resolution than Auger spectroscopy. A kinetic analysis of the segregation rate of Mn at 450 °C was consistent with bulk diffusion of these elements in ferrite and resulting segregation. Further similar results on Mn segregation to grain boundaries has been reported in other studies [59–67]. Differences among the various results are due to the different alloys and the corresponding chemical potentials for Mn and also due to site competition effects.

4.2. Segregation-induced nanoscale martensite to austenite reversion versus growth of retained nanoaustenite

The results show that segregation engineering can be used in martensitic steel to design nanosized phase transformation layers (Fig. 1). More specifically, the joint TEM and APT analysis reveals strong Mn segregation to the martensite grain boundaries and the subsequent formation of an intergranular austenitic layer at a prior martensite grain boundary in an Fe–9 at.% Mn steel after quenching and subsequent ageing at 450 °C for 48 h (Figs. 4–9).

An important point in that context is whether some of the transformation events described above might be austenite growth effects, proceeding from tiny layers of retained austenite, rather than generic austenite reversion plus growth phenomena as claimed here. Indeed, there are various points in support of austenite reversion without retained austenite nuclei, as discussed below.

In a previous paper about the mechanical properties associated with this nanoscale martensite to austenite reversion [2] we showed that in a 9 wt.% Mn containing alloy no retained austenite was found after quenching. However, it should be noted that the EBSD resolution limit in this work was only about 40–45 nm and, hence, smaller retained austenite layers might have not been detected.

However, there is an important additional argument. When considering Figs. 7 and 8 of the present work in conjunction with Table 1 we observe that the segregation that precedes austenite formation applies not only to the austenite stabilizing elements Mn and Ni but also to the ferrite stabilizing elements Ti, Si, and Mo. The strength of segregation can be quantified in terms of the element-specific enrichment factor $k_i = C_i^{GB}/C_i^{T}$, where C_i^{GB} is the atomic concentration of element i at the grain boundary and C_i^{T} is the atomic bulk concentration of the same element. For Mn it is 2.3 and for Ni 1.7 (both austenite stabilizing elements) (Fig. 10). For the ferrite stabilizing elements the grain boundary enrichment factors are even much higher, 2.3 for Mo, 5.2 for Ti, and 14 for Si. This observation suggests that the decorated region is originally indeed a martensite grain boundary and not a very thin layer of retained austenite. If it had been retained austenite no segregation of ferrite stabilizers such as Ti, Mo, and Si would have occurred.

Irrespective of these hints supporting segregation-stimulated nanoscale martensite to austenite reversion for the cases shown above, it cannot be ruled out that retained nanoscale austenite might also occur and act as a template for further growth of austenite.

Since, however, we did not find retained nanoaustenite layering in any of the 9 wt.% Mn specimens we additionally studied such interfaces in an alloy containing 12 wt.% Mn exposed to exactly the same quench and heat treatment cycle (Fe–12Mn–2Ni–0.15Al–1Mo–1Ti–0.05Si–0.01 wt.%, Fe–12.2Mn–1.9Ni–0.3Al–0.6Mo–1.2Ti at.%). This composition yields slightly higher austenite stability and, hence, increases the probability of finding retained austenite after quenching.

Fig. 12 shows both cases of interfaces (segregation decorated martensite–austenite–martensite interface region and retained austenite plus austenite growth region) in the 12 wt.% Mn alloy after the same tempering treatment as used for the 9 wt.% Mn alloy (450 °C, 48 h). Fig. 12a shows a case of a martensite–austenite–martensite interface region similar to the examples shown in Figs. 8 and 9a for the 9 wt.% Mn steel. The data reveal the segregation of both austenite and ferrite stabilizing elements, indicating that no retained austenite had been present on the former martensite–martensite interface.

Fig. 12b shows an interface region where retained austenite was present after quenching and served as a template for austenite reversion via growth. This transformed interface region in the 12% Mn alloy, originating from an inherited retained austenite nanolayer (~3 nm), reveals a profoundly different Mn profile compared with those austenite interface layers that were formed by reversion without the aid of retained austenite during the heat treatment in both the 9 and 12 wt.% Mn alloys. The retained austenite observed in Fig. 12b in the 3 nm centre region of the Mn profile reveals a Mn concentration that corresponds to the original austenite equilibrium concentration (12 wt.% Mn), while the reversed austenite that is subsequently formed on top of it during 450 °C ageing follows the local Mn partitioning values between austenite and martensite. This means that the Mn content of the reversed austenite is much higher, since the negligible diffusion of Mn at 450 °C for 48 h in austenite suppresses equilibration of Mn inside the retained plus reversed austenite region. This effect, known as kinetic freezing [56], leads to a situation where retained austenite regions that act as nucleation centres for austenite reversion have a much lower Mn content than the austenite that is formed on top of them. In contrast, the austenite reversion layers newly formed by Mn decoration plus phase transformation (such as claimed in this paper) have a homogeneous Mn concentration and do not reveal such Mn gradients as observed for the case of the retained plus reversed austenite scenario.

Comparison of these examples in the 12 wt.% Mn alloy reveals that the two cases, segregation decorated martensite–austenite–martensite interface regions on the one hand and retained austenite plus austenite reversion regions on the other, represent profoundly thermodynamically and kinetically different situations which can be clearly distinguished from each other by APT.

Another important feature of the retained austenite nanolayers that we observed in the 12% Mn model alloys (but not in the 9% Mn alloys) is that the retained austenite does not form any precipitates during subsequent ageing.

4.3. General evaluation of segregation-induced nanoscale martensite to austenite reversion

Structural and chemical characterization of the newly formed intergranular austenite layer shows two important features: first, at least one of the two austenite films is in a K-S orientation relationship with its adjacent martensite grain, as proved by TEM-SAD (Figs. 4 and 5). Second, the austenite film had a very high Mn concentration of about 22–24 at.%, revealed by APT, while the abutting martensite region contained only 4–6 at.% Mn. This value is below the average bulk Mn concentration of 9 at.% in martensite. The Mn concentrations on either side of the martensite–austenite interface are close to the thermodynamically expected partitioning of Mn between bcc and fcc for this alloy, as will be discussed in more detail below (Figs. 7–9).

Similar austenite formation mechanisms of or at interfacial layers have been discussed in the literature: Krauss and Cohen [51] studied martensite to austenite reverse transformation in a Fe–33.5 wt.% Ni steel; Breedis [52] observed that in Fe–Cr–Ni steels reversed austenite contained twins inside the parent martensitic phase; Jana and Wayman [53], Kessler and Pitsch [54], and Guy et al. [55] observed that the martensite to austenite transformation for different stainless steels is time dependent, i.e. the austenite fraction increases as a function of annealing time. This effect of Mn segregation to interfaces and subsequent austenite growth in re-austenitization scenarios was also studied by APT by Dmitrieva et al. [56] on a Mn-based maraging transformation-induced plasticity (TRIP) steel and by Yuan et al. [68] on an Fe–Cr–C stainless cutting steel. Dmitrieva et al. [56] found partitioning of Mn at martensite–austenite phase boundaries in two phase (retained γ austenite, α' martensite) Fe–Mn steel. Based on thermodynamic and diffusion simulations using DICTRA they concluded that a new layer of reversed austenite had grown at a martensite–austenite interface.

Lee et al. [69] studied the reverse transformation from martensite to austenite in an Fe–3Si–13Cr–7Ni (wt.%) martensitic stainless steel. They observed that below a heating rate of 10 K s^{-1} the reverse transformation of martensite to austenite occurred by diffusion, whereas it proceeded by diffusionless shear for heating rates above 10 K s^{-1}. After the reversion treatment at low temperature thin austenite films were observed along the martensite lath boundaries,

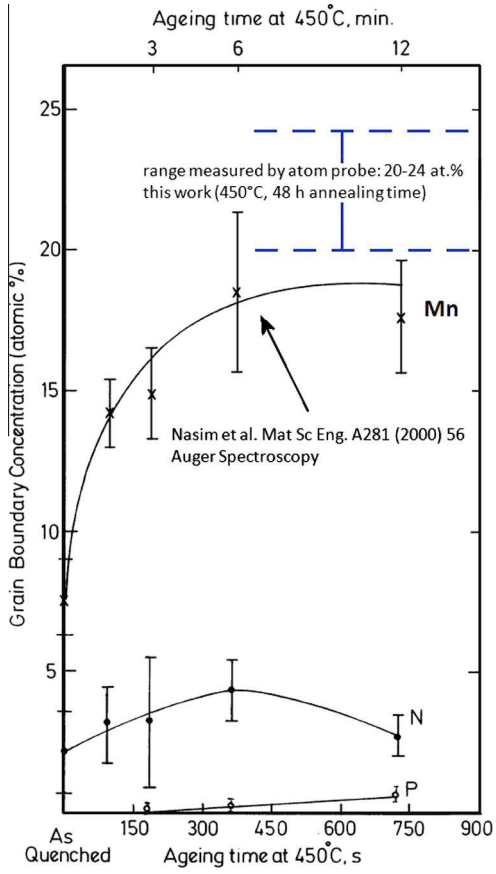

Fig. 11. Grain boundary segregation in an Fe–8Mn alloy upon ageing at 450 °C measured by Nasim et al. [58] using Auger spectroscopy. The Mn grain boundary segregation data (about 20–24 at.% Mn) measured in this work by APT on an Fe–9 at.% Mn martensite alloy were added to the original data taken from the work of Nasim et al. [58].

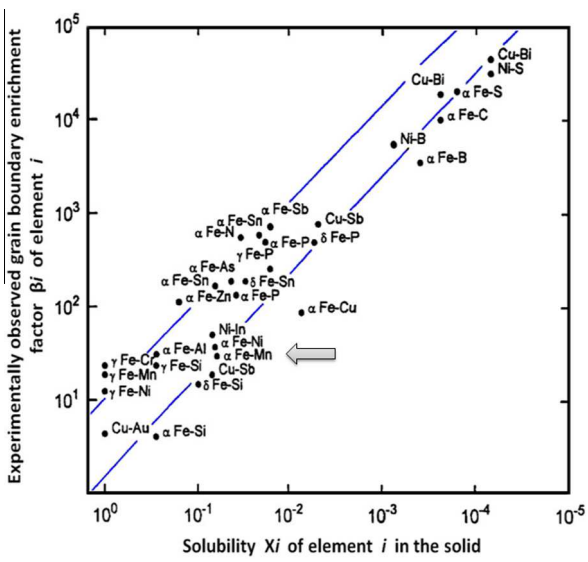

Fig. 10. Grain boundary segregation data compiled from values published by Shea and Hondros [14–18] and Lejček [20–22,25] and, for Mn in martensite, our own measurements determined by APT, here and in previous works [38,56] (arrow).

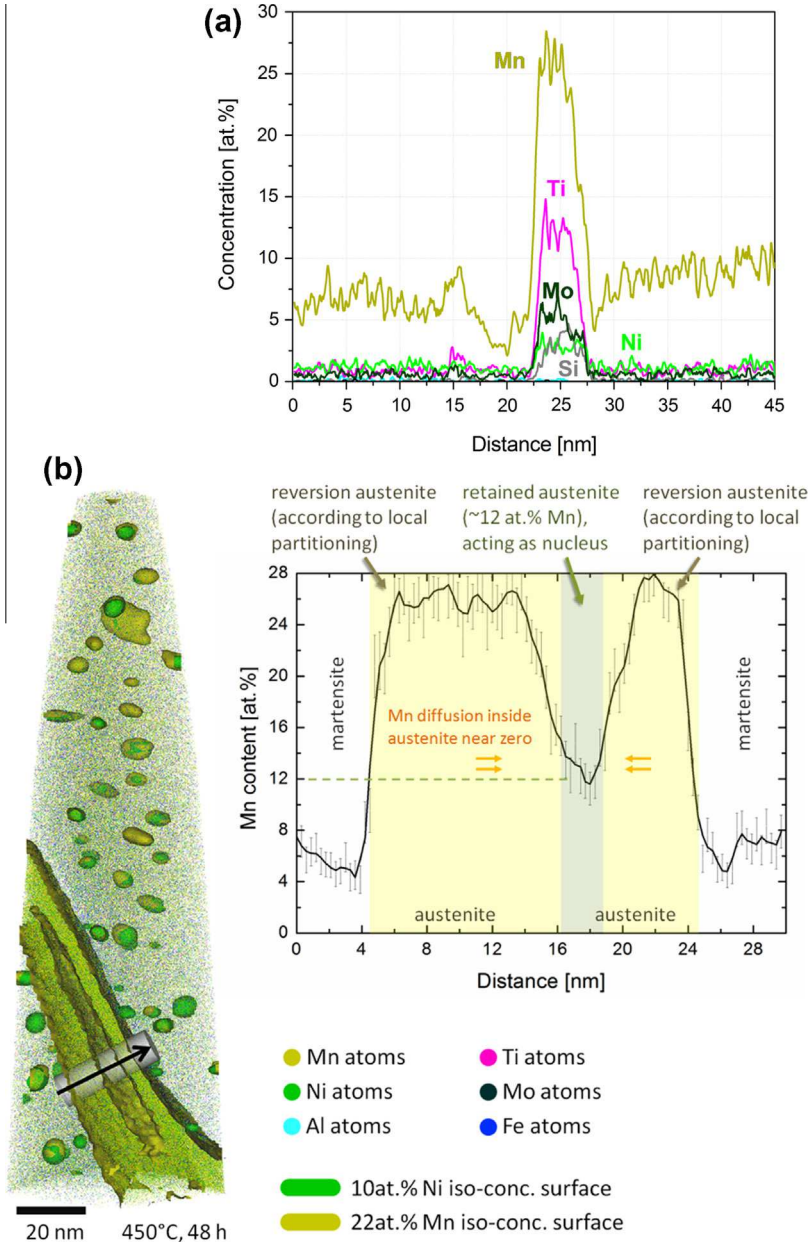

Fig. 12. (a) Chemical gradients across a martensite–austenite–martensite interface region after tempering (450 °C, 48 h). The nominal composition of the alloy is 12.2 Mn, 1.9 Ni, 0.6 Mo, 1.2 Ti, 0.3 Al (at.%). The data reveal the segregation of both austenite and ferrite stabilizing elements. (b) The interface region in a 12.2 Mn, 1.9 Ni, 0.6 Mo, 1.2 Ti, 0.3 Al (at.%) alloy where retained austenite was present after quenching, serving as a nucleation site for austenite reversion via growth. The retained austenite nanolayer is ~3 nm thick and has a Mn concentration that corresponds to the original austenite equilibrium concentration (12 wt.% Mn) while the reversed austenite subsequently formed on top of it during the 450 °C ageing follows the local Mn partitioning values between austenite and martensite. Therefore, the Mn content of the reversed austenite is much higher, since the negligible diffusion of Mn at 450 °C for 48 h in austenite impedes equilibration of Mn inside the retained plus reversed austenite region (kinetic freezing [56]).

while reversion treatment at high temperatures produced granular austenite inside the martensite laths, in addition to austenite films.

Using internal friction and dynamic modulus experiments Montaneri [70] noted a necessary period of incubation before the start of reverse martensite to austenite transformation in a 95% cold rolled and annealed AISI 304 stainless steel. He interpreted the incubation period in terms of the diffusion of interstitial atoms to internal interfaces and to stress relaxation of the parent martensite phase during the heat treatment.

Tomimura et al. [71] observed that austenite can nucleate at martensite grain boundaries and grow when annealed for longer times. The phenomenon depended on alloy composition. They further reported that the initial shape of the newly formed austenite depends on the morphology of the parent martensite phase. For the case of cold rolled lath martensite the austenite nucleated at

lath boundaries and intersections and expanded from there into the martensite. For the case that the parent martensite has a dislocation cell-containing lath structure, equiaxed fine austenite grains formed at the martensite grain boundaries.

Rajasekhara and Karjalainen have also observed these phenomena in several cold rolled and annealed stainless steel grades [73,74]. They suggested that the time dependence of these reversion phenomena could be understood in terms of a diffusion-assisted mechanism. They concluded that martensite to austenite reversion occurs over a wide temperature range, leads to the formation of defect-free austenitic grains which can further grow in size with time, and leads to a wide austenite grain size distribution. The authors also noted that secondary phase precipitates can occur in competition with austenite formation, as was observed by Dmitrieva et al. [56] and Yuan et al. [68] in corresponding APT experiments.

The current results also show that the time dependence of the martensite to austenite reversion also depends on the preceding Mn segregation step that leads to intense decoration of the martensite grain boundaries, as documented in Figs. 7–11.

Dmitrieva et al. [56] reported that the diffusion length of Mn at 450 °C after 48 h is as small as 90 nm in martensite, hence the time dependence of the observed segregation-assisted reversion. Fig. 9a shows the situation just before onset of the transformation, with a 22–23 at.% segregation of Mn to the martensite grain boundary.

Thuillier et al. [75] observed partitioning of C at austenite–martensite phase boundaries in a Fe–0.18C–1.72Mn steel, annealed for 50 s at 700 °C, by APT. They assumed that this partitioning triggers the austenite–ferrite phase transformation at 700 °C.

Mun et al. [76] detected the nucleation of fine (~20 nm) austenite particles at grain and lath boundaries in an Fe–8Mn–7Ni (wt.%) steel after 30 min ageing at 450 °C. By TEM-EDS analysis they found that Mn and Ni were not segregated at grain boundaries in the as-quenched condition and that after ageing these elements were partitioned in the reverted austenite particles [76]. Wilson and Nasim et al. [58,77] reported the segregation of Mn to martensite lath boundaries and prior austenite boundaries during annealing at 450 °C in Fe–8Mn and Fe–8Mn–7Ni (wt.%) alloys. During short annealing times (10–12 min) the authors observed high Mn concentrations of up to 20 wt.% at the grain boundaries using Auger electron spectroscopy at fractured surfaces. These segregation zones were only a few monolayers thick. After annealing for 199 h at 450 °C they observed martensite to austenite reversion at prior austenite grain boundaries, martensite lath boundaries, and triple junctions. While annealing for less than 10 h at 450 °C led to severe grain boundary embrittlement, longer annealing times resulted in increased impact toughness with increasing amount of reversed austenite, as documented by XRD analysis.

A similar effect was described by Morris et al. [78] in bcc Fe–Ni steel. They explained the increase in toughness observed after annealing by the formation of nanoscale austenite precipitates at grain boundaries. They showed that these tiny austenite precipitates inhibited cleavage fracture and led to a lowering of the ductile–brittle transition temperature [78]. Podder et al. [79] found thin layers of austenite in Fe–C–Ni–Si steel to be more stable against martensitic transformation than blocky austenite. Yuan et al. [68] made similar observations on nanoscale austenite layers in Fe–Cr–C martensite steels.

Regarding the crystallographic relationship between martensite and austenite formed by reverse transformation, various groups have studied the crystallographic orientations of the abutting phases as well as austenite memory effects [80–87].

Finally, in a different context, the formation of local interface layers was suggested by Guttmann [88] and by Harmer et al. [89–91]. The latter group observed different interfacial phases, which they referred to as complexions [89–91]. Since the observed phases were assumed to be intrinsically unstable [91] the authors concluded that the phases were stabilized by the interface, although this specific effect of stabilization of a new intermediate interface phase only through its formation at an existing interface has not yet been confirmed for the case of austenite reversion.

These various studies [51–87] on martensite to austenite reversion demonstrated not only the possibility to form confined re-austenized layers in martensitic reversion steels but also reported the beneficial effect of such local transformations on the mechanical behaviour.

However, the direct observation of such nanosized phenomena requires the joint use of advanced characterization methods to a gain deeper insight into the effects of both compositional and structural inhomogeneities. In particular, the relationship between local chemical gradients and local structural transformations requires the combined quantitative analysis of chemistry (APT) and structure (TEM) at near atomic level.

In the following sections we discuss our current experimental observations in terms of two types of thermodynamic–kinetic approaches, namely the adsorption isotherm in conjunction with classical heterogeneous nucleation models for allotriomorphic transformations at interfaces and a phase field model that considers segregation plus a gradual phase transition to austenite at martensite grain boundaries.

The goal of the analysis was to elucidate the basic principle behind the mechanism of such nanoscale phase transformation at segregation decorated martensite grain boundaries. If we understand this mechanism it can be used to design ductile martensitic alloys that contain mechanically compliant nanostructures at the interfaces [2,38,56,68]. It is expected that such a principle can be extended to any type of alloy where solute- and stress-dependent phase transformations can occur.

4.4. Thermodynamic analysis of austenite formation and Mn partitioning

Analysis of the thermodynamic phase compositions and stabilities at 450 °C, considering the nominal chemical composition of the alloy, were conducted using Thermo-Calc® [38]. The analysis reveals an austenite (fcc) phase fraction of 24.68 mol.% in thermodynamic equilibrium (Fig. 13). The analysis predicts Mn partitioning between the newly formed austenite and the surrounding martensite (treated as bcc phase) with 2.83 at.% in the bcc phase and 28.44 at.% in the fcc phase (austenite).

Recently, Dmitrieva et al. [56] reported that the mean diffusion path of Mn during annealing at 450 °C for 48 h was about 13 nm in defect-free ferrite. When fitting the corresponding partitioning diffusion simulations to the experimentally observed APT results the authors identified a somewhat higher mean diffusion path of about 90 nm for near cubic Fe–Mn martensite. Obviously, this value is far too low to reach a global thermodynamic equilibrium for Mn during the ageing heat treatment in the current case (48 h, 450 °C).

The fact that the observed local APT concentration profiles taken across the martensite–austenite–martensite interface region fit surprisingly well to the equilibrium concentrations that were estimated by Thermo-Calc at 450 °C means that the system approaches thermodynamic equilibrium locally, i.e. within the range of the corresponding diffusion paths (a few nanometres) of the elements involved (Figs. 7 and 8). This means that the Thermo-Calc predictions provide a good match with the observed local partitioning behaviour of Mn between martensite and austenite. The term "local" here refers to a length scale that is of the order of the diffusion path of Mn in martensite, 13–90 nm at 450 °C (48 h).

To estimate the chemical driving force for austenite formation at 450 °C in thermodynamic equilibrium on the basis for these results we analysed three different thermodynamic scenarios. These did not include structural defects, but only the thermochemical driving forces under different constraints. The first scenario assumed a simplified binary Fe–Mn system where we gradually change the (local) Mn concentration in the martensite. The chemical driving force for local transformation to austenite was then calculated as a function of the Mn content (Fig. 14, black curve). As shown in this graph, for Mn concentrations above 13.3 at.% a thermo-chemical driving force exists to form austenite at 450 °C in binary Fe–Mn. The motivation for this scenario is the general observation of local Mn enrichment in this study, as well as in previous studies, in near binary Fe–Mn systems [2,56,58,77].

In the second scenario all major alloying elements (Mn, Mo, Ti, Ni, and Si) in the current alloy were considered. We assumed no in-phase chemical gradients but all elements were assumed to be homogeneously distributed, except for Mn, which was again systematically varied (Fig. 14, blue curve). The concentrations of the different alloying elements are given by the nominal composition of the alloy. The calculations showed a similar trend as in the binary Fe–Mn system (first scenario). At Mn concentrations above 12.4 at.% the transformation from martensite to austenite was thermodynamically favourable.

The third scenario included the experimentally (APT) observed local enrichments of Si, Ni, Mo, and Ti (see Figs. 8 and 9) instead of the nominal values. More specifically, the measured concentrations of Si, Ni, and Ti averaged over a length of 2 nm across the enriched zone were considered. Again, only the Mn concentration was varied to evaluate the trend when compared with the first and second scenarios (Fig. 14, green curve). Due to the presence of bcc stabilizing elements (Si, Mo, and Ti) in the third scenario higher Mn concentrations (>15.3 at.%) were required to obtain a chemical driving force that was sufficient for martensite to austenite transformation. Generally the energy gain through the formation of austenite is lower than in the first and second scenarios, but still significant.

From these estimates we conclude that in all three cases there is a strong chemical driving force for the formation of austenite. Therefore, the presence of austenite is thermodynamically favourable at the enriched interface layer, despite accumulation of the bcc stabilizing elements.

Within that context it should be considered that calculation of the local thermodynamics, as outlined above, only serves as a rough estimate of the segregation effect on the chemical driving forces for martensite to austenite reversion. This is due to the fact that the thermodynamic potentials apply only for the martensite (ferrite) bulk grain, not for the corresponding martensite grain boundaries. In the absence of a consistent thermodynamic model for multi-component grain boundaries we therefore use the

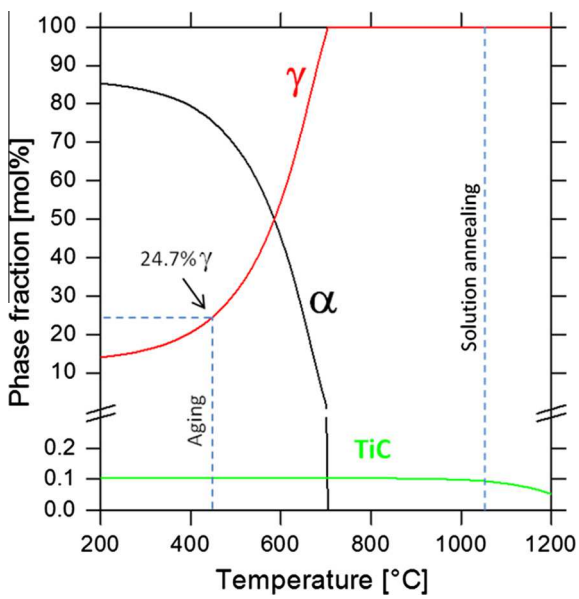

Fig. 13. Equilibrium volume fraction of the phases as a function of temperature predicted by Thermo-Calc®. The dotted line shows the 450 °C tempering applied in the present case.

thermodynamic calculation only as an approximation for the local driving force due to segregation. A more consistent approach to the conjunction of segregation and phase transformation is presented later in Section 4.8 using a phase field model.

4.5. Rules for designing martensite with nanoscaled austenite interface layers

Following the observations of Dmitrieva et al. [56], Yuan et al. [68], Ma et al. [72], and Rajasekhara and Karjalainen [73,74] we can establish a set of design rules for segregation-assisted nanoscale martensite to austenite reverse transformation at decorated martensite interfaces (segregation engineering). According to these rules solutes used for segregation should fulfil three criteria: first, they should reveal a sufficiently high tendency to segregate at grain boundaries in the chosen matrix material in order to provide large concentration differences between the matrix and the defect [20–22]; second, solute enrichment should reduce the transformation temperature (from martensite to austenite in this case); third, the solute should prefer local segregation to an interface over precipitation of a competing third phase inside the matrix (e.g. carbide formation rather than carbon segregation to grain boundaries). When these criteria are fulfilled and the difference in solute concentration between the matrix and the decorated lattice defect is high enough local phase transformation in these confined and nanoscaled defect regions can be stimulated via changes in the thermodynamic state variables (temperature change, pressure change, or mechanical loading). The state change must be adjusted in such a way that the solute-depleted matrix is not transformed, but only the segregation zones.

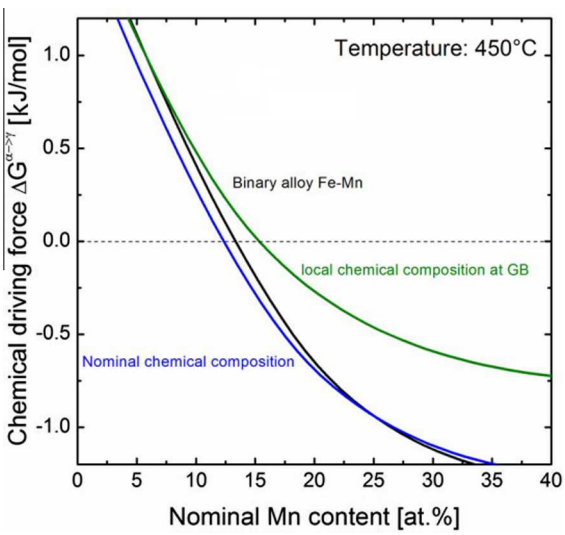

Fig. 14. Thermodynamic driving force for reverse α′–γ transformation as a function of the Mn concentration when considering: (i) binary Fe–Mn (black curve); (ii) homogeneous distribution of the major alloying elements Ni, Si, Ti, and Mo; (iii) local enrichment of Ni, Si, Ti, and Mo (as determined from APT measurements, Figs. 7 and 8).

4.6. Orientation relationship between reversed austenite and martensite

Bulk reverse α′–γ martensitic transformation phenomena have been studied before, for example in Fe–Ni metastable austenitic stainless steels and in two phase martensitic–austenitic steels with a substantial (>10 vol.%) fraction of retained austenite [80–94]. During mechanical treatment deformation-induced α′ martensite is formed in such alloys. Subsequent annealing between the A_s (reverse transformation start temperature) and A_f (reverse transformation finish temperature) after deformation leads to martensite to austenite reversion. The orientation relationship between strain-induced α′ martensite and reversed γ austenite is the same K-S orientation relationship observed for the strain-induced γ–α′ martensitic transformation [95,96]. This thermomechanically induced process has been used to form fine grained austenite structures [80,97]. In these studies the metastable austenite was thermally formed from strain-induced α′ martensite, i.e. no partitioning was required to induce the reverse α′–γ martensitic transformation. In contrast, in the present study in which we subjected an Fe–Mn martensite to a 450 °C maraging heat treatment, diffusion leads at first to grain boundary segregation of Mn, which is one of the necessary preconditions for a highly localized reverse α′–γ transformation effect [56,68,102]. Hence, in the investigated martensite only local chemical enrichments at defects (here grain boundaries) and elastic strain relaxation (see below) stabilize the formation of nanoscale allotriomorphic γ austenite.

The observation of a K-S relationship in this study does not necessarily prove that martensite to austenite reversion followed a displacive, i.e. diffusionless transformation mechanism. Such an orientation relationship can also be created by diffusional epitaxial growth of austenite into martensite, or even by a combination of both mechanisms [80,97].

4.7. Heterogeneous nucleation of nanoscale martensite to austenite reversion at a straight martensite grain boundary: spherical cap and pillbox nucleation models

The Thermo-Calc results for the different segregation scenarios (different local compositions) reveal that a thermodynamic driving force for austenite formation exists in the analysed interface region (see Section 4.2) (Fig. 14). As stated above, certain limitations as to the validity of these values have to be considered as they apply to bulk martensite rather than to martensite grain boundaries (see Section 4.4). Here we use the approximate driving force based on the measured APT concentrations (case (iii) in Fig. 14) in discussing heterogeneous nucleation of the martensite to austenite reversion phenomenon in the present alloy.

Nucleation of reversed austenite has been addressed by various authors [73,74,80–94,96,97–101]. For the case of a nucleus comprising two spherical caps the nucleation

barrier $\Delta G^*(T, x)$, for a double spherical cap martensite to austenite transformation nucleus formed at a straight martensite grain boundary (Fig. 15) is:

$$\Delta G^*(T,x) = \frac{4(b\gamma_{\text{M-A}} - a\gamma_{\text{M-M}})^3}{27c^2(\Delta g_{\text{chem}}(T,x))^2} \quad (1)$$

where $\Delta g_{\text{chem}}(T, x)$ is the change in chemical free energy per unit volume associated with transformation from the parent phase martensite to austenite as a function of Mn concentration x and temperature T (Figs. 13 and 14) [96,98]. The geometrical constant a quantifies the martensite grain boundary area removed during reversion, b is the newly formed austenite–martensite interface area, and c describes the volume of the austenite nucleus [96] (Fig. 15). The shape parameters a, b, and c depend on the geometry of the nucleating crystal [98–105]. We use the results of Clemm and Fisher [98], who established relationships between these shape and volume factors and the dihedral angle for three typical nuclei shapes with two, three and four grain junctions, respectively, with the parent martensite phase (Fig. 15).

These models show that the activation energy for austenite reversion at four and three grain austenite–martensite junctions is lower than that for the two grain austenite–martensite junctions. This is in line with earlier observations on the current alloy which showed re-austenitization at triple points [56].

From Fig. 15 we extract the local mechanical equilibrium equation:

$$k = \cos\theta = (\gamma_{\text{M-M}})/(2\gamma_{\text{M-A}}) \quad (2)$$

For the case of a double spherical cap austenite nucleus located on a planar martensite grain boundary the geometrical parameters amount to [96,98]:

$$\begin{aligned} a &= \pi(1-k^2) \\ b &= 4\pi(1-k) \\ c &= (2\pi/3)(2-3k+k^2) \end{aligned} \quad (3)$$

In our case (Figs. 4–9 and 14) the interface energy balance includes three contributions, removal of the martensite–martensite interface ($\gamma_{\text{M-M}}$), formation of the new martensite–austenite interface ($\gamma_{\text{M-A}}$) and, in the present specific case, formation of an internal austenite–austenite interface ($\gamma_{\text{A-A}}$). Three aspects deserve attention in this context. First, the austenite–austenite interface, as observed in Fig. 4, is neglected here at first, since it does not appear as a necessary precondition for nucleation. Second, the removed martensite–martensite grain boundary is decorated by ~22–23.5 at.% Mn. Following the Gibbs adsorption isotherm this means that the interface energy is lower compared with a non-decorated martensite grain boundary. Third, martensite grain boundaries differ in terms of their misorientation and energy. More specifically, a lower energy value must be used for the case that re-austenitization occurs at a small angle lath martensite boundary [9–13,32] than for the case of reversion at a former austenite grain boundary (martensite high angle grain boundary). The differences between the two cases were discussed by Nakada et al. [80,97]. The latter scenario (high angle martensite grain boundary, i.e. former austenite grain boundary) differs from the former one (low angle martensite grain boundary, lath interface) in terms of the higher misorientation between the martensite grains and, hence, higher interface energy. Grain boundaries with higher misorientations also have potentially higher segregation contents [22,25].

Since martensite is elastically highly strained and the newly formed austenite with its higher atomic packing density allows release of that strain energy we rewrite the nucleation expression for the case of a double spherical cap nucleus (Eq. (1), Fig. 15a) as:

$$\Delta G^*(T,x) = \frac{4(b\gamma_{\text{M-A}} - a\gamma_{\text{M-M}})^3}{27c^2(\Delta g_{\text{chem}}(T,x) + \Delta g_{\text{elast}})^2} \quad (4)$$

where Δg_{elast} is the change in elastic free energy per unit volume associated with transformation from the parent martensite phase to the product austenite phase [80,97]. It provides an energy gain (relaxation) term upon martensite reversion to austenite.

To calculate the nucleation barrier according to Eq. (4) we use the thermodynamic driving force of case (iii) in Fig. 14 for austenite formation according to the APT observations of ~24 at.% Mn at the martensite interface, i.e. a value of Δg_{chem} (450 °C, 24 at.% Mn) = 0.85 kJ mol^{-1} (corresponding to 121 MJ m^{-3} when using the molar volume of Fe–Mn, $V_m = 7.1 \times 10^{-6}$ m^3 mol^{-1}.

Regarding the interface energy contributions we use data from earlier works [102–109] as upper and lower bounds, respectively, which have shown that the martensite high angle grain boundary energy can be approximated as 1.3 J m^{-2}. Nakada suggested a somewhat smaller value of 1.1 J m^{-2} for a martensite high angle grain boundary and 0.2 J m^{-2} for a lath martensite (low angle) boundary [97]. Furthermore, since the martensite–austenite interfaces in our current example are at least in one case crystallographically related through the K-S relationship [102–109] we assume that the energy of the newly formed austenite–martensite interface is equal to that of the eliminated martensite–martensite grain boundary. This is in accordance with the work of Gjostein et al. [95], who experimentally observed that the bcc/fcc interfacial energy ratio for Fe–C alloys is approximately 1. Hence, we assume a lower bound estimate of the nucleation barrier values of 1.3 J m^{-2} for both the martensite–martensite and the austenite–martensite interfaces and a lower-bound estimate of 0.2 J m^{-2} for both interfaces (martensite–martensite lath boundary and K-S martensite–austenite interface). These are important parameters since the value of the enumerator in Eq. (4) depends sensitively not only on the shape of the austenite nucleus but also on the energy balance between the newly formed austenite and the removed martensite interfaces [98,103–106].

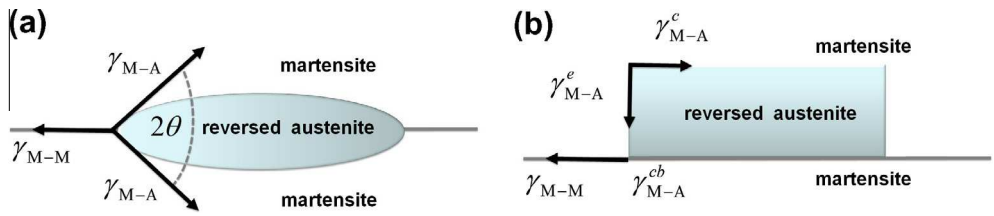

Fig. 15. Two classes of nucleation models for the formation of allotriomorphic austenite at the interface between two martensite grains. (a) Double spherical cap shape of a martensite to austenite reversion nucleus formed on a segregation decorated martensite grain boundary. γ_{M-M}, martensite–martensite interface energy; γ_{M-A}, martensite–austenite interface energy [96,98]. (b) Coherent pillbox nucleus according to Lange et al. [104,105]. In this model all interfaces are assumed to be of low energy and coherent. γ^{e}_{M-A}, martensite–austenite interface edge energy; γ^{cb}_{M-A}, facet energy in the grain boundary plane; γ^{c}_{M-A}, energy within the upper martensite grain; γ_{M-M} energy associated with the martensite–martensite interface.

For the case where the austenite grain was transformed from martensite through a single crystallographic variant mode the relaxation gain in elastic strain energy density can be estimated by:

$$\Delta g_{\text{elast}} = \frac{1}{2}E_I\varepsilon_I^2 + \frac{1}{2}E_{II}\varepsilon_{II}^2 + \frac{1}{2}E_{III}\varepsilon_{III}^2 \tag{5}$$

where E_I, E_{II}, and E_{III} are single variant values for the Young's modulus in each of the loaded lattice directions (one [0 0 1] and two [110] directions), and the corresponding elastic strains ε_I, ε_{II}, and ε_{III} are 0.139 (expansion), 0.07 (contraction), and 0.014 (contraction) [111]. The elastic constants E_I, E_{II}, and E_{III} are 132.1, 220.8, and 220.8 GPa, respectively, which give a value of 1839 MJ m^{-3} for the elastic strain energy density [111]. This is an upper bound estimate due to some degree of martensite strain relaxation during the 450 °C heat treatment that precedes reversion. Also, the single variant transformation scenario provides the highest elastic misfit. Similar results for the elastic energy density contribution were calculated by Nakada et al. [97] by finite element simulations. For a lower bound estimate of the elastic energy gain upon reversion we use a relaxed and multi-orientation variant scenario. This is a minimized elastic mismatch case, where the elastic energy density is one order of magnitude smaller than for the single variant case, since multiple variants can mutually cancel out their elastic energy contributions.

Some further aspects have to be considered at this stage. First, at the beginning we neglected, for reasons of generalization, the fact that a new austenite–austenite grain boundary was formed inside the nucleus (Fig. 3). In order to include this additional interface in the energy balance for the case of a double spherical cap nucleus we rewrote Eq. (4) as:

$$\Delta G^*(T,x) = \frac{4(b\gamma_{M-A} + a(\gamma_{A-A} - \gamma_{M-M}))^3}{27c^2(\Delta g_{\text{chem}}(T,x) + \Delta g_{\text{elast}})^2} \tag{6}$$

where γ_{A-A} is the grain boundary energy for the newly formed austenite–austenite interface. When we assume that the interface energy γ_{A-A} is identical to that of the martensite–martensite grain boundary γ_{B-B} and correct for the local force equilibrium, i.e. $k = \gamma_{M-M}/(2\gamma_{M-A} - \gamma_{A-A})$, we obtain slightly increased nucleation barriers.

A second point concerns the nucleus shape. Previous authors discussed, for the case of ferrite nucleation [103–105], the influence of different nucleation shapes on steady-state nucleation rates. The double spherical cap and pillbox shaped nucleation variants shown in Fig. 15 were introduced in earlier works as two prototype cases for a number of more complex shaped and truncated nucleation variants (Fig. 16). In these earlier works not only were the respective shape factors for the different nuclei introduced, but the specific assumption that the associated interfaces for the pillbox shaped nucleation variants were coherent and had very small interface energies was also used. Under such conditions coherent pillbox nuclei were suggested to have smaller nucleation barriers compared with spherical cup shaped nuclei (Fig. 16).

The wide spectrum of nucleation model variants and parameter ranges outlined above only allows the assessment of upper and lower bounds for the nucleation barriers. Depending on the nucleus shape, elastic energy release, chemical driving force, and interface energies we obtained a lower bound value of 0.05 eV and upper bound values of several electron volts for the martensite to austenite nucleation barrier.

In that sense we can in principle interpret our experimental observations of segregation- and elasticity-assisted martensite to austenite reversion at lath martensite boundaries in terms of heterogeneous nucleation. The main reasons for the low nucleation barrier are, first, the high equilibrium segregation of Mn to the lath martensite boundary, leading to a high chemical driving force [56,112], second, the low energy of the newly formed K-S austenite–martensite interface, and, third, the high gain in elastic energy density associated with the martensite to austenite transformation.

An important concern associated with this approach lies in using classical heterogeneous nucleation models for a phase reversion phenomenon that is characterized by the size of only a few atomic layers. At such small dimensions certain homogeneity assumptions inherent in classical nucleation theory may be generally questioned. For instance, at near atomic scales ledges and specific local crystallographic facets may play an important role in the local interface energy values involved. Also, at near atomic scales elastic relaxation occurs, i.e. elastic transitions across

interfaces are not sharp but can be smeared over several atomic layers. Dealing with energies and associated nucleation phenomena at such small scales hence requires more sophisticated methods to be considered in the future. Suitable approaches could, for instance, include energy calculations for specific interface structures by electron density functional simulations or corresponding molecular relaxation studies in conjunction with bond order potential functions. The predicted potential landscape could then be used, for instance, to inform corresponding kinetic Monte Carlo, phase field, or phase field crystal simulations of martensite to austenite or related allotriomorphic transformations at interfaces.

4.8. Phase field kinetic analysis of the formation of interfacial austenite layers

Above we have shown that some aspects associated with the observed reversion phenomenon can in principle be explained in terms of conventional heterogeneous nucleation, but we have also discussed the limitations of this concept. Here we analyse the kinetics associated with the current experimental observations in terms of a gradual segregation–transformation sequence using a phase field model concept. In this view the segregation of Mn is due to the individual solubility of the martensite grain boundaries. The associated formation of austenite at these decorated interfaces occurs, as in all Ginzburg–Landau based formalisms, in the form of a gradual transformation as a function of the local segregation content [113,114].

The phase field approach is generally suited to treat microstructural–kinetic problems, such as solute redistribution, interface motion, and phase transformation, on mesoscopic length scales [113–115]. For the present analysis a particular merit of the phase field approach is that it incorporates a continuous and smooth variation in structural order, e.g. over a diffuse interface between abutting phases. We take advantage of this latter characteristic to represent a grain boundary as a partially disordered (amorphous) region of finite thickness, which inherits its thermodynamic properties from a fractional composition of the coexisting amorphous and solid phases. In this way the model is capable of describing the initial stage of grain boundary segregation and gradual formation of the austenite layer. A brief description of the model is next given, while full technical details will be provided in a subsequent work.

The model is based on a multi-phase field approach [116] considering a crystalline fcc phase, a bcc phase, and an amorphous phase in the Fe–Mn system. The bcc phase represents the Fe–Mn martensite matrix. The motivation for incorporation of the amorphous phase is to provide a conceptual basis for quantification of the partial structural disorder at the martensite grain boundaries. In such an interface concept structural disorder at the grain boundary relative to the surrounding crystalline matrix is here realized by assuming non-zero values of the structure phase

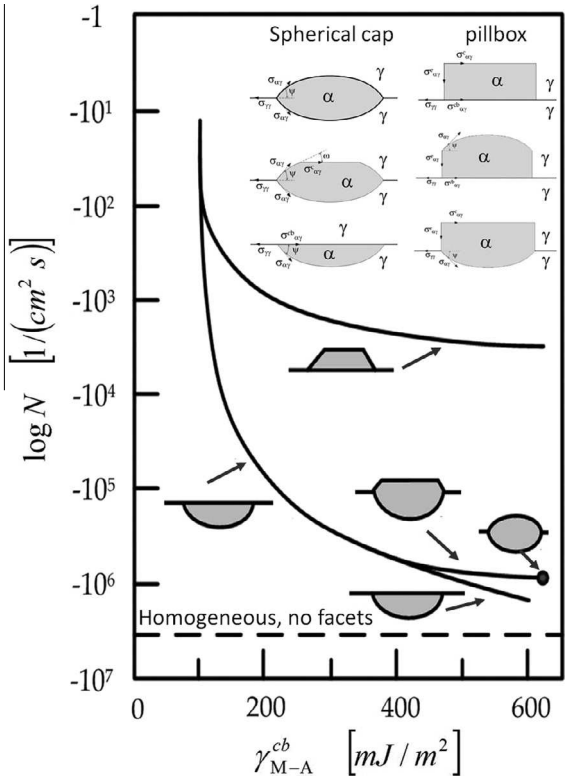

Fig. 16. Estimates of the steady-state nucleation rates for different models of allotriomorphic ferrite formation according to Russell [103], Clemm and Fisher [98], and Lange et al. [104,105] as a function of the interfacial ferrite–austenite energy. The authors used different shape factors and truncated variants for spherical cup and pillbox shaped nucleation. They also made the specific assumption that the associated newly formed interfaces for the pillbox shaped nucleation variants were coherent and hence had small interfacial energies.

field variable that represents the amorphous phase. Inside the martensitic Fe–Mn matrix the structure variable for the amorphous phase assumes a zero value. At the position of the martensite interface it assumes a non-zero value which characterizes the structural disturbance of the bcc martensite area at the position of the grain boundary (Fig. 17).

In this way the thermodynamic properties of the grain boundary are linked to those of the amorphous and solid phases and, hence, the initial stage of segregation is modelled without a need to use additional adjustable parameters that are specific to the problem of grain boundary segregation. The Gibbs free energies of the bcc, fcc, and amorphous phases as used in the present analyses are based on thermodynamic assessment of the Fe–Mn system by Huang [117], whereas the diffusivities are those considered by Dmitrieva et al. [56].

Fig. 17 shows the results of one-dimensional simulations for Fe–10 at.% Mn aged at 450 °C. In this case the austenite layer has a single orientation, and the nominal interfacial energy between the bcc and fcc phases is 0.1 J m^{-2}. Within the first hours of ageing the grain boundary is predominantly marked by a partially disordered layer, as manifested by a peak in the phase field profile of the amorphous

phase. There is no indication of austenite formation at the grain boundary during this time, although the differences in structural order, and hence in the chemical potential, result in the segregation of Mn to the grain boundary. As the peak concentration increases beyond a certain level the phase field variable corresponding to the fcc phase starts to rise from zero at the grain boundary. For the present example this occurs after about 10 h of ageing at 450 °C. From this point onwards the fcc phase field variable (p3) rises continuously to reach the maximum value of unity at the centre of the (diffuse) grain boundary region. This marks the formation of a thermodynamically stable austenite layer, which completely replaces the initial martensite grain boundary at this position. The austenite layer reaches a thickness of ~4 nm after 48 h ageing at 450 °C, in reasonable consistence with the experimental observations. The Mn concentration at this stage falls from the peak value of 33 at.% Mn back to an equilibrium value of about 28 at.% Mn, whereas the adjacent bcc grains reach a minimum of about 6 at.% Mn. Moreover, simulations show that the formation of an austenite double layer is only possible for certain combinations of interfacial properties. An example of this is shown in Fig. 18, where the nominal fcc/bcc interfacial energy is reduced from 0.1 to 0.05 J m^{-2}, and the misorientation between the two austenite layers is kept below 15°. This suggests that formation of a double layer is only possible on certain grain boundaries which are characterized by a specific orientation relationship.

Based on our experimental and theoretical results we propose the following model for the nucleation and growth process of the observed interfacial austenitic layers.

Three main effects determine formation of the observed interfacial austenite layers: (i) chemical segregation; (ii) high elastic distortion at the martensite grain boundaries; (iii) heterogeneous nucleation of austenite.

The strong segregation of Mn to and around the grain boundary (a strain field due to martensitic distortion) as well as the high elastic distortion at the grain boundaries jointly provide a high driving force to form austenite during ageing. The energetically preferable place for heterogeneous austenite nucleation is at the martensite interfaces. It should be emphasized that the phase field approach used above to understand the interplay between segregation and re-austenitization does not include generic nucleation,

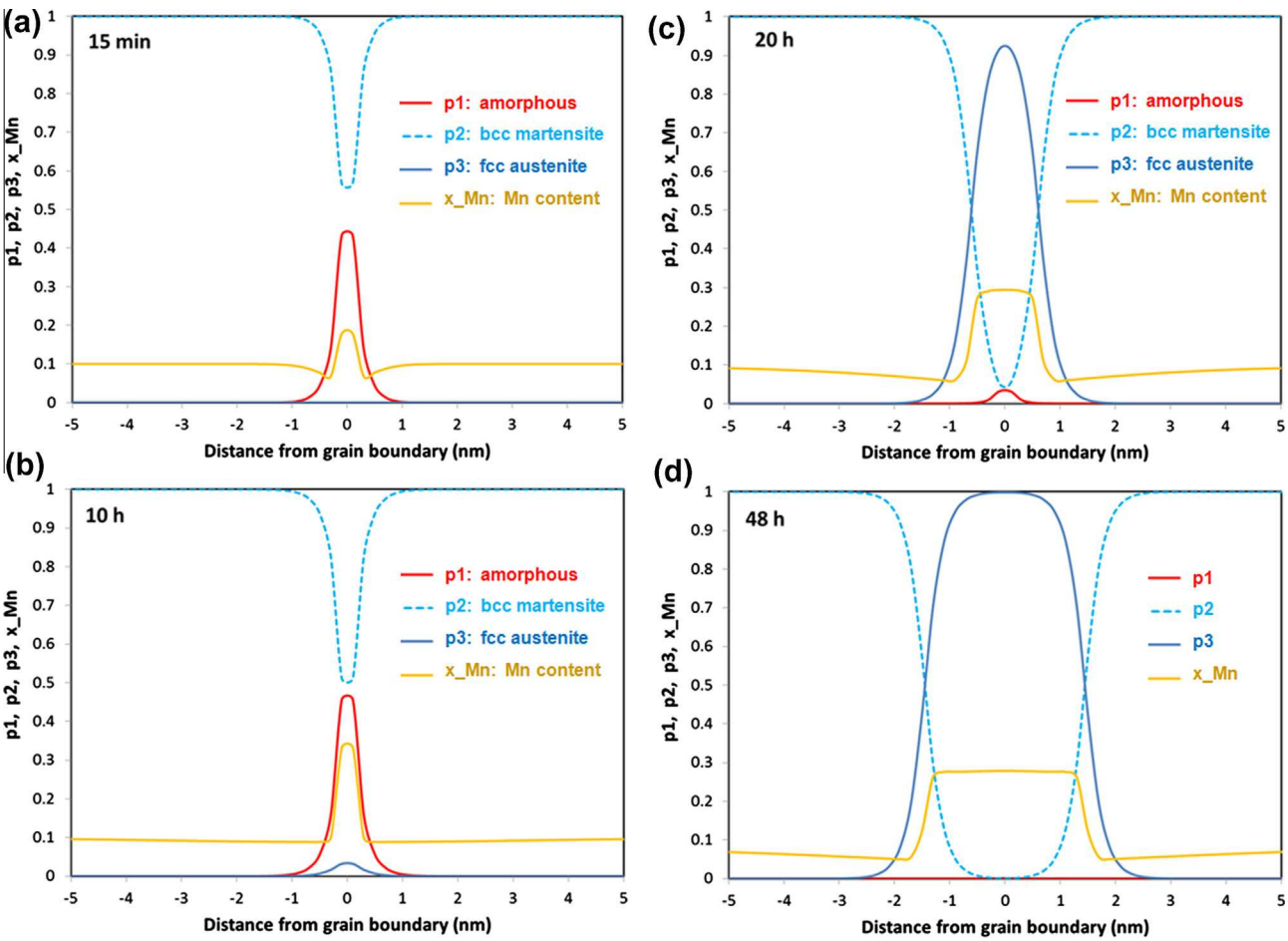

Fig. 17. Temporal evolution of the composition and phase field variables (p1, amorphous phase representing partial disorder at the initial martensite grain boundary; p2, bcc Fe–Mn martensite phase; p3, fcc reversed austenite phase) across the boundary of two abutting bcc (martensite) grains in Fe–10 at.% Mn, calculated for 450 °C. The austenite layer is assumed to have a single crystal orientation.

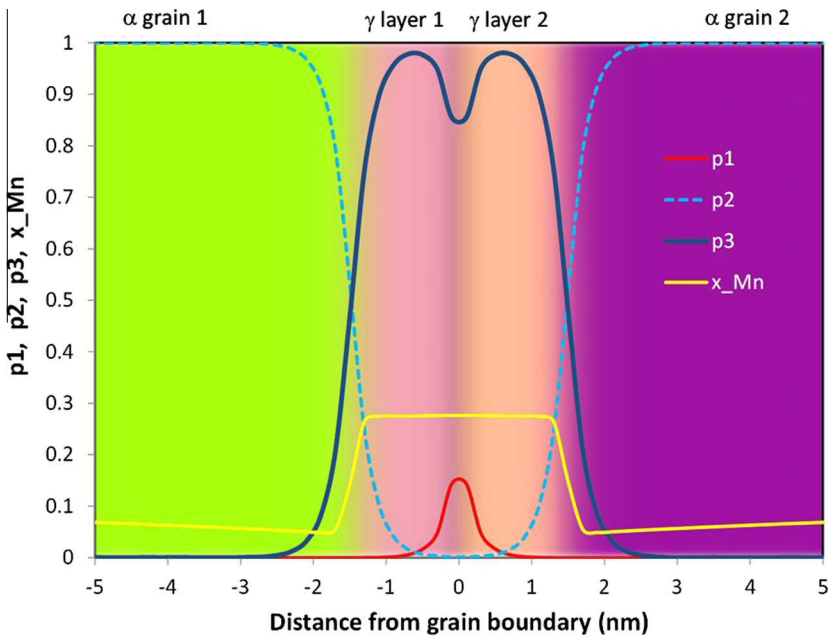

Fig. 18. Phase field simulation of the formation of a reversed austenite double layer between two abutting martensite crystals. Calculated profiles of field variables across the grain boundary in Fe–10 at.% Mn aged for 48 h at 450 °C. Different background colors indicate different crystal orientations (p1, amorphous phase representing partial disorder at the martensite grain boundary, p2, bcc Fe–Mn martensite phase; p3, fcc reversed austenite phase).

but rather anticipates that tiny Mn-rich clusters already exist as austenite precursors in the martensite interfaces. This means that we assume that local Mn-rich structural elements in the grain boundary might support formation of the fcc phase. Hence, the phase field model essentially explains segregation, further partitioning of Mn, and the associated growth of these precursor islands.

Another relevant point is the interfacial energies of the newly formed martensite–austenite grain boundaries, which are generally assumed to be equal to or lower than high angle martensite–martensite grain boundaries [95]. The observation of a K-S orientation relationship, which is generally assumed to be energetically favourable, shows that interface energy minimization is a relevant point.

Lateral growth along the grain boundary is supported by the existing Mn concentration profile. Therefore, enrichment of Mn at and adjacent to the grain boundary leads to the formation of some layers of austenite with a certain phenomenological analogy to complexions observed in ceramics [89–91]. Since austenite is a stable phase in the Fe–Mn system for the observed high Mn concentrations the so formed austenite layers grow into the adjacent grains. The growth is limited by the bulk diffusion of Mn inside the martensite.

5. Conclusions

The formation of nanosized austenitic reversion layers at segregation decorated martensite grain boundaries in Fe–9Mn–1.9Ni–0.6Mo–1.1Ti–0.33Al–0.1Si–0.05C (at.%) steel was observed using TEM and APT. The interfacial austenite had a double layered structure. A K-S orientation between one of these austenitic layers and its adjacent martensite grain was found. A thermodynamic and kinetic analysis of the local chemical composition across the layers was conducted and revealed that the thin austenite is a thermodynamically stable phase under the current boundary conditions.

The observation that the formation of nanosized austenite reversion layers can be stimulated at segregation decorated martensite lath boundaries opens a new pathway in the design of ductile martensite. For this purpose the solutes that segregate to the martensite grain boundaries should be elements with a high segregation tendency, that reduce the transformation temperature (from martensite to austenite), that prefer segregation over bulk precipitation (e.g. carbide), and that promote local phase transformation at grain boundaries, i.e. martensite to austenite reversion confined to GBs in the current case. We refer to this new approach of manipulating the structure and composition of grain boundaries via segregation and phase transformation as "segregation engineering".

We have shown that the formation of nanoscale austenite layers at decorated martensite interfaces can in principle be explained in terms of heterogeneous nucleation. Rough estimates provide nucleation barriers of about 0.5–1 eV at 450 °C with 24 at.% Mn segregation. The main reasons for this low nucleation energy is the high segregation of Mn to the lath martensite boundary, the low energy of the newly formed K-S austenite–martensite interface and, specifically, the high elastic relaxation energy of the martensite associated with the transformation. A more gradual model of the diffusion and transformation processes associated with interface martensite reversion was obtained using

a phase field approach, by which we described the martensite grain boundary as a mixture of a disordered phase with an individual Mn solubility and the bcc martensite phase. Upon sufficient Mn segregation the austenite phase gradually becomes stabilized at the grain boundary.

Acknowledgements

The PhD fellowship funding of J. Millán, by the Fundación Gran Mariscal de Ayacucho (Fundayacucho-Venezuela) in cooperation with the German Student Exchange Service is gratefully acknowledged.

References

[1] Ritchie RO. Nat Mater 2011;10:817.
[2] Raabe D, Ponge D, Dmitrieva O, Sander B. Adv Eng Mater 2009;11:547.
[3] Gutierrez-Urrutia I, Raabe D. Acta Mater 2012;60:5791.
[4] Song R, Ponge D, Raabe D, Kaspar R. Acta Mater 2005;53:845.
[5] Song R, Ponge D, Raabe D, Speer JG, Matlock DK. Mater Sci Eng A 2006;441:1.
[6] Hodgson PD, Hickson MR, Gibbs RK. Scripta Mater 1999;40:1179.
[7] Song R, Ponge D, Raabe D. Acta Mater 2005;53:4881.
[8] Hickson MR, Hurley PJ, Gibbs RK, Kelly GL, Hodgson PD. Metall Mater Trans A 2002;33:1019.
[9] Krauss G. Mater Sci Eng A 1999;273–275:40.
[10] Ueji R, Tsuji N, Minamino Y, Koizumi Y. Acta Mater 2002;50:4177.
[11] Ohmura T, Minora AM, Stacha EA, Morris JW. J Mater Res 2004;19:3626.
[12] Kitahara H, Ueji R, Tsuji N, Minamino Y. Acta Mater 2006;54:1279.
[13] Morito S, Huang X, Furuhara T, Maki T, Hansen N. Acta Mater 2006;54:5323.
[14] Shea MP. Surf Sci 1975;53:168.
[15] McLean D. Grain boundaries in metals. Oxford: Oxford University Press; 1957.
[16] Seah MP, Hondros ED. Proc R Soc Lond A 1973;335:191.
[17] Hondros ED. Proc R Soc Lond A 1965;286:479.
[18] Hondros ED, Seah MP. Metall Trans A 1977;8:1363.
[19] Langmuir I. J Am Chem Soc 1918;40:1361.
[20] Hoffman S, Lejcek P. Interface Sci 1996;3:241.
[21] Lejček P, Hofmann S. Crit Rev Solid State Mater Sci 1995;20:1.
[22] Lejcek P, Hoffman S. Crit Rev Solid State Mater Sci 2008;33:133.
[23] Liu F, Kirchheim R. Scripta Mater 2004;51:521.
[24] Wynblatt PW, Chatain D. Metall Mater Trans A 2006;37:2595.
[25] Lejček P, Hofmann S, Paidar V. Acta Mater 2003;51:3951.
[26] Kirchheim R. Acta Mater 2002;50:413.
[27] Kirchheim R. Acta Mater 2007;55:5129.
[28] Weissmüller J. Nanostruct Mater 1993;3:261.
[29] Weissmüller J. J Mater Res 1994;9:4.
[30] Seah MP. Acta Metall 1977;25:345.
[31] Grabke HJ. ISIJ Int 1989;29:529.
[32] Morito S, Tanaka H, Konishi R, Furuhara T, Maki T. Acta Mater 2003;51:1789.
[33] Watanabe T. Res Mech 1984;11:47.
[34] Watanabe T, Kitamure S, Karashima S. Acta Metall 1980;28:455.
[35] Watanabe T, Tsurekawa S. Acta Mater 1999;47:4171.
[36] Randle V. Acta Mater 2004;52:4067.
[37] Randle V. Acta Mater 1999;47:4187.
[38] Raabe D, Ponge D, Dmitrieva O, Sander B. Scripta Mater 2009;60:1141.
[39] Thermo-Calc Software AB and Foundation of Computational Thermodynamics. ThermoCalc users' guide, version S. Stockholm: Thermo-Calc Software AB; 2011.
[40] Thermo-Calc Software AB. TCFE6 – TCS steels/Fe-alloys database, version 6.2. Stockholm: Thermo-Calc Software AB.
[41] Miller MK, Cerezo A, Hetherington MG, Smith GDW. Atom probe field ion microscopy. Oxford: Oxford University Press; 1996.
[42] Danoix F, Bémont E, Maugis P, Blavette D. Adv Eng Mater 2006;8:1202.
[43] Li YJ, Choi PP, Borchers C, Westerkamp S, Goto S, Raabe D, et al. Acta Mater 2011;59:3965.
[44] Sauvage X, Copreaux J, Danoix F, Blavette D. Philos Mag A 2000;80:781.
[45] Raabe D, Choi PP, Li YJ, Kostka A, Sauvage X, Lecouturier F, et al. MRS Bull 2010;35:982.
[46] Marquis EA, Choi PP, Danoix F, Kruska K, Lozano-Perez S, Ponge D, et al. Microsc Today 2012;20:44.
[47] Sauvage X, Lefebvre W, Genevois C, Ohsaki S, Hono K. Scripta Mater 2009;60:1056.
[48] Hong MH, Reynolds Jr WT, Tarui T, Hono K. Metall Mater Trans A 1999;30:717.
[49] Hono K, Ohnuma M, Murayama M, Nishida S, Yoshie A. Scripta Mater 2001;44:977.
[50] Li YJ, Choi PP, Goto S, Borchers C, Raabe D, Kirchheim R. Acta Mater 2012;60:4005.
[51] Krauss G, Cohen M. Trans Am Inst Metal Eng 1962;224:1212.
[52] Breedis JF. Trans Am Inst Eng 1966;236:218.
[53] Jana S, Wayman CM. Trans Am Inst Eng 1967;239:1187.
[54] Kessler H, Pitsch W. Acta Metall 1967;15:401.
[55] Guy KB, Butler EP, West DRF. Met Sci 1983;17:167.
[56] Dmitrieva O, Ponge D, Inden G, Millán J, Choi PP, Sietsma J, et al. Acta Mater 2011;59:364.
[57] Nikbakht F, Nasim M, Davies C, Wilson EA, Adrian H. Mater Sci Technol 2010;26:552.
[58] Nasim M, Edwards BC, Wilson EA. Mater Sci Eng A 2000;281:56.
[59] Weng YQ, McMahon CJ. Mater Sci Technol 1987;3:207.
[60] Heo NH. Acta Mater 1996;44:3015.
[61] Maier P, Faulkner RG. Mater Charact 2003;51:49.
[62] Grabke HJ, Hennesen K, Moeller R, Wei W. Scripta Metall 1987;21:1329.
[63] Krahe PR, Guttmann M. Scripta Metall 1973;7:387.
[64] Lee HJ, Morris JW. Metall Trans A 1983;14:913.
[65] Bolton JD, Petty ER, Allen GB. Metall Trans 1971;2:2915.
[66] Guo H, Purdy GR. Met Mater Trans A 2008;39A:950.
[67] Mega T, Shimomura J, Seto K. Mater Trans JIM 1996;37:323.
[68] Yuan L, Ponge D, Wittig J, Choi P, Jiminez JA, Raabe D. Acta Mater 2012;60:2790.
[69] Lee Y-K, Shin H-C, Leem D-S, Choi J-Y, Jin W, Choi C-S. Mater Sci Technol 2003;19:393.
[70] Montaneri R. Z Metallk 1990;81-H2:114.
[71] Tomimura K, Takaki S, Tokunaga Y. ISIJ Int 1991;31:1431.
[72] Ma Y, Jin J-E, Lee Y-K. Scripta Mater 2005;52:1311.
[73] Rajasekhara S, Karjalainen LP, Kyröläinen A, Ferreira PJ. Mater Sci Eng A 2010;527:1986.
[74] Somani MC, Juntunen P, Karjalainen LP, Misra RDK, Kyröläinen A. Metall Mater Trans 2009;40A:729.
[75] Thuillier O, Danoix F, Gouné M, Blavette D. Scripta Mater 2006;55:1071.
[76] Mun SH, Watanabe M, Li X, Oh K, Williams DB, Lee HC. Metall Mater Trans A 2002;33A:1057.
[77] Wilson EA. Metall Mater Trans A 2004;35A:352.
[78] Morris JW, Guo Z, Krenn CR, Kim YH. ISIJ Int 2011;41:599.
[79] Podder AS, Lonardelli I, Molinari A, Bhadeshia HKDH. Proc R Soc A 2011;467:3141.
[80] Law NC, Edmonds DV. Metall Trans A 1980;11A:33.
[81] Middleton CJ, Form GW. Met Sci 1975;9:521.
[82] Kimmins ST, Gooch DJ. Met Sci 1983;17:519.

[83] Hoshimi K, Ashida Y, Hato H, Atagi R, Ishihara K, Nakamura H. Tetsu-to-Hagane 1978;64:595.
[84] Zhang Y, Jing X, Lou BZ, Shen FS, Cui FZ. J Mater Sci 1999;34:3291.
[85] Matsuda S, Okamura Y. Trans ISIJ 1974;14:444.
[86] Yasuno T, Koganei A, Kuribayashi K, Hasegawa T, Horiuchi R. ISIJ Int 1996;36:595.
[87] Maki T, Morimoto H, Tamura I. Tetsu-to-Hagane 1979;65:1598.
[88] Guttmann M. Metall Trans A 1977;8:1383.
[89] Dillon SJ, Tang M, Carter WC, Harmer MP. Acta Mater 2007;55:6208.
[90] Harmer MP. Science 2011;332:182.
[91] Luo J, Cheng H, Asl KM, Kiely CJ, Harmer MP. Science 2011;333:1730.
[92] Nakada N, Tsuchiyama T, Takaki S, Miyano N. ISIJ Int 2011;51:299.
[93] Somani MC, Juntunen P, Karjalainen LP, Misra RDK, Kyröläinen A. Metall Mater Trans A 2009;40:729.
[94] Tomimura K, Takaki S, Tokuunaga Y. ISIJ Int 1991;31:1431.
[95] Gjostein NA, Domain HA, Aaronson HI, Eichen E. Acta Metall 1966;14:1637.
[96] Rajasekhara S, Ferreira PJ. Acta Mater 2011;59:738.
[97] Nakada N, Tsuchiyama T, Takaki S, Hashizume S. ISIJ Int 2007;47:1527.
[98] Clemm PC, Fisher JC. Acta Metall 1955;3:70.
[99] Kurdjumov GV, Khandros LC. Dokl Akad Nauk SSSR 1949;66:211.
[100] Hollomon JH, Turnbull D. Prog Met Phys 1953;4:333.
[101] Kaufman L, Cohen M. Prog Met Phys 1958;7:165.
[102] Bowkett MW, Keown SR, Harries DR. Met Sci 1982;16:499.
[103] Russell KC. Acta Metall 1969;17:1123.
[104] Lange WF, Enomoto M, Aaronson HI. Int Mater Rev 1989;34:125.
[105] Lange WF, Enomoto M, Aaronson HI. Metall Trans A 1988;19:427.
[106] Reed RC, Bhadeshia HKDH. Mater Sci Technol 1992;8:421.
[107] Offerman SE, van Dijk NH, Sietsma J, Grigull S, Lauridsen EM, Margulies L, et al. Science 2002;298:1003.
[108] Nishiyama Z. Martensitic transformations. New York: Academic Press; 1978.
[109] Shibuta Y, Takamoto S, Suzuki T. Comput Mater Sci 2009;44:1025.
[110] Mangonon PL, Thomas G. Metall Mater Trans 1970;1A:1587.
[111] Takaki S, Fukunaga K, Syarif J, Tsuchiyama T. Mater Trans 2004;45:2245.
[112] Odqvist J, Hillert M, Agren. Acta Mater 2002;50:3211.
[113] Chen LQ. Annu Rev Mater Res 2002;32:113.
[114] Ma N, Dregia SA, Wang Y. Acta Mater 2003;51:3687.
[115] Boettinger WJ, Warren JA, Beckermann C, Karma A. Annu Rev Mater Res 2002;32:163.
[116] Folch R, Plapp M. Phys Rev E 2005;72:011602.
[117] Huang W. Calphad 1989;13:243.